Understanding and Controlling the Magnetic and Optical Properties in van der Waals Semiconductors

Kaichen Xie

A dissertation

submitted in partial fulfillment of the

requirements for the degree of

Doctor of Philosophy

University of Washington

2024

Reading Committee:

Ting Cao, Chair

Di Xiao

Xiaodong Xu

Mark S. Rudner

Program Authorized to Offer Degree:

Materials Science and Engineering

University of Washington

Abstract

Understanding and Controlling the Magnetic and Optical Properties in van der Waals Semiconductors

Kaichen Xie

Chair of the Supervisory Committee:

Professor Ting Cao

Materials Science and Engineering

Within the broad spectrum of two-dimensional (2D) materials, 2D van der Waals (vdW) magnetic semiconductors are distinguished by their novel properties, which stem from the weak yet tunable interlayer magnetic interactions, adding an entirely new magnetic degree of freedom to vdW interfacial engineering. In this dissertation, we discuss the understanding and prediction of the magnetic and optical properties of vdW magnetic semiconductors employing *ab initio* methods alongside other theoretical and computational techniques. This dissertation is organized as follows:

- In Chapter 1, we provide a brief introduction to the theoretical and computational methods that compute the quasiparticle and exciton properties of materials, and the recent advancements in the field of 2D magnetic semiconductors.

- In Chapter 2, we focus on exploring the magneto-excitonic coupling in a prototypical 2D vdW magnet CrSBr utilizing *ab initio* calculations.[1] We uncover the anisotropic Wannier nature of the 2D excitons in few-layer CrSBr and the entanglement of excitons between vdW layers of this material.
- In Chapter 3, we present several mechanical approaches to harnessing the power of magneto-electronic coupling in 2D vdW magnet CrSBr.[2,3] Our qualitative analysis attributes the effects of these mechanical tuning knobs on magnetic properties to subtle alterations in bond geometry.
- In Chapter 4, we investigate the intriguing potential for manipulating magnetic phases in 2D magnets through interfacial charge transfer in heterostructures of magnetic and nonmagnetic layers.[4] We unveil a transition towards the ferromagnetic phase by stacking antiferromagnetic bilayer CrSBr on graphene and by electrostatic doping. We further demonstrate that the phase transition is a spin-canting process.
- In Chapter 5, we establish a theoretical framework to investigate the ultrafast optical control of excitonic structures. We demonstrate coherent optical field as a powerful tool to manipulate the excitonic properties in 2D materials. From our calculations, we find that the dark and bright excitons can be coherently coupled, resulting in novel absorption features as a function of frequency.

Contents

List of Figures

List of Tables

Acknowledgements

First of all, I would like to thank my advisor Professor Ting Cao. Back in 2019, I found myself at a crossroads during the first year of my Ph.D. program and it was partially by chance I was suggested to talk to Ting, who had just joined our department and was searching for graduate students. I cannot overstate how fortunate I feel to have had the opportunity to work with and learn from Ting. Ting guided me into the forefront of condensed matter physics and materials science. His exceptional scientific intuition and great enthusiasm for research have always inspired me and shaped me. As my advisor, Ting has always been encouraging, supportive and responsive throughout my research journey, particularly during the hard times of the pandemic. Whenever I encountered obstacles, I knew I could rely on Ting's vast knowledge and experience to highlight ideas I had overlooked. I am deeply grateful to Ting for inspiring me to think independently and critically about physics, and for enlightening me on my future career path.

Secondly, I would like to extend my sincere thanks to my committee members, Professor Di Xiao, Professor Xiaodong Xu, and Professor Mark. S. Rudner. Di has been incredibly supportive throughout my graduate studies, and I have really enjoyed our discussions about both physics and life. Xiaodong has remarkably expanded my understanding of experimental observations, and I have greatly benefited from his lectures and discussions. Mark's profound understanding of fundamental physics in solid-state systems has bolstered my own theoretical understanding of my work.

My sincere thanks go to my colleagues: Jimin, Tharindu, Shivesh, Yusen, Lingnan, Wenqin, Yueyao, Xiao-Wei, Chong, Xiaoyu, Yafei. You are all incredible. We have built a collaborative

environment within our research group. It has been a privilege to work with and learn from you. I will always cherish the experience we shared.

I have been fortunate to collaborate with numerous brilliant researchers over the years, and I want to thank all of them for sharing their expertise: Nathan Wilson, John Cenker, Eric Anderson and Jordan Fonseca from Xiaodong Xu's group; my collaborators at University of Washington, Di Xiao, Jiun-Haw Chu, and David S. Ginger; my collaborators at Columbia University, Evan J. Telford, Kihong Lee, Avalon Dismukes, Xavier Roy, Xiaoyang Zhu, and Cory R. Dean; Yunfan Guo from Jing Kong's group. This dissertation would not have been possible without their tremendous efforts.

Yuhuan, I can't believe it has been eight years since we first met at the start of our graduate studies. We have walked down this long path together and we have made it through. I can only wish you all the best. You, Yifei and I have shared many common hobbies and spent countless hours together during our free time. Thank you for your emotional support, encouragement, and care in this challenging journey.

Lastly, I want to express my deepest appreciation to my parents and grandparents. Thank you for your unconditional and selfless love, patience, and belief in me. Your constant support and understanding have been a continual source of strength for me.

To my parents, Yuqiong Chen and Fangde Xie,

for their endless love and support.

Chapter 1

Introduction

In this chapter, we will firstly introduce several *ab initio* methods used throughout this dissertation in calculating the electronic and optical properties of materials: density functional theory (DFT) for ground-state properties, the GW method for quasiparticle (QP) properties, and the GW plus Bethe–Salpeter Equation (GW-BSE) method for optical properties. The second part is a brief introduction to vdW magnetic semiconductors.

1.1 Density Functional Theory

The *ab initio* DFT approach is a numerical method to simulate real materials and predict the ground-state properties of molecules and solids. The idea of DFT is developed by Hohenberg and Kohn,[5] followed by the derivation of a set of equations by Kohn and Sham,[6] which has been implemented in software packages such as VASP,[7] Quantum Espresso,[8] etc. We will give a brief introduction to the physical theories lying under this approach.

1.1.1 Kohn–Sham Equation

From Born–Oppenheimer approximation,[9] the position of the nuclei can be considered fixed with respect to the electrons, as the nuclei are much heavier than the electrons and consequently move more slowly than the electrons. Therefore, we treat the nuclei and electrons as separate problems and the Hamiltonian for the electrons is given by (in atomic units $\hbar = m = e = 1$)

$$H = \sum_i \left[-\frac{1}{2}\nabla_i^2 + V_{\text{ext}}(\mathbf{r}_i) \right] + \frac{1}{2}\sum_{i \neq j} \frac{1}{|\mathbf{r}_i - \mathbf{r}_j|} \tag{1.1}$$

where the three terms in the Hamiltonian represent the electron kinetic energies, the local external potential (e.g., the field from the nuclei), and the Coulomb interactions between pairs of electrons, respectively. Here we have neglected spin-orbit coupling and other relativistic effects. The electron Hamiltonian follows the time-independent Schrödinger equation

$$H\Psi(\mathbf{r}_1, \mathbf{r}_2, \dots, \mathbf{r}_N) = E\Psi(\mathbf{r}_1, \mathbf{r}_2, \dots, \mathbf{r}_N) \tag{1.2}$$

$\Psi = \Psi(\mathbf{r}_1, \mathbf{r}_2, \dots, \mathbf{r}_N)$ is the electron wave function, which is a function of the spatial coordinates of N electrons. E is energy eigenvalue. However, solving the full wave function Ψ for practical materials are extremely hard as the computational effort scales exponentially with the system size. Therefore, approximate theories have been developed in an effort to derive effective single-particle approximations for the Coulomb term, and among these approaches, DFT stands out as one of the most frequently employed approaches.

The basis of DFT are the two theorems first proved by Hohenberg and Kohn in 1960s.[5] The first theorem states that the ground-state electron density uniquely determines all properties, including the energy and wave function, of the ground state. Here, the ground-state energy E, which can be expressed as $E[n(\mathbf{r})]$, is a functional of $n(\mathbf{r})$. The second theorem finds that electron density can be found by minimizing the energy functional, which gives us a prescription to find the relevant electron density. A practical approach was developed by Kohn and Sham,[6] where the complicated N-electron wave function $\Psi(\mathbf{r}_1, \mathbf{r}_2, \dots, \mathbf{r}_N)$ and the associated Schrödinger equation are replaced by a formulation that uses the much simpler electron density $n(\mathbf{r})$. $n(\mathbf{r})$ can be written in terms of the occupied single-electron wave functions ψ_i as

$$n(\mathbf{r}) = \sum_{i=1}^{N} |\psi_i(\mathbf{r})|^2 \tag{1.3}$$

Here, $n(\mathbf{r})$, which is a function of only three degrees of freedom (one spatial coordinates), carries information from the full solution to the Schrödinger equation, which is a function of N spatial coordinates. A set of self-consistent, single-particle equations, known as the Kohn–Sham equation, has the form

$$\left[-\frac{1}{2}\nabla^2 + V_{\text{ext}}(\mathbf{r}) + V_H(\mathbf{r}) + V_{\text{XC}}(\mathbf{r})\right]\psi_i(\mathbf{r}) = \varepsilon_i\psi_i(\mathbf{r}) \tag{1.4}$$

Here, $V_{\text{ext}}(\mathbf{r})$ includes the interaction between an electron and all nuclei, also appearing in Eq. (1.1). $V_H(\mathbf{r})$ is the Hartree potential and has the form

$$V_H(\mathbf{r}) = \int v(\mathbf{r}, \mathbf{r}')n(\mathbf{r}')\, d\mathbf{r}' \tag{1.5}$$

with the bare Coulomb interaction $v(\mathbf{r}, \mathbf{r}') = 1/|\mathbf{r} - \mathbf{r}'|$. The Hartree potential defines the Coulomb repulsion between one electron and the total electron density defined by all electrons in the system. The Hartree potential includes a self-interaction contribution. As the currently described electron in the Kohn–Sham equation is also part of the total electron density, part of V_H involves a Coulomb interaction between the electron and itself. The correction for this self-interaction is one of several effects that count for the final potential in the Kohn–Sham equation, V_{XC}, which defines exchange and correlation contributions to the single-electron equation. V_{XC} is defined as the functional derivative of the exchange-correlation energy

$$V_{\text{XC}}(\mathbf{r}) = \frac{\delta E_{\text{XC}}[n(\mathbf{r})]}{\delta n(\mathbf{r})} \tag{1.6}$$

1.1.2 Exchange-Correlation Functional

In fact, the general form of the exchange-correlation functional should be nonlocal. However, such form is unknown in most cases. We will briefly introduce two common approaches to approximate the exchange-correlation functional, the local density approximation (LDA) and the generalized gradient approximation (GGA). LDA is parameterized using the one-to-one correspondence between total energy density and electron density in the uniform electron gas.[10,11] The exchange-correlation functional at each electron density is approximated as

$$E_{\mathrm{XC}}^{\mathrm{LDA}}[n] = \int n(\mathbf{r})\epsilon_{\mathrm{XC}}(n(\mathbf{r}))d\mathbf{r} \tag{1.7}$$

where $\epsilon_{\mathrm{XC}}(n)$ is the exchange and correlation energy per electron of a uniform electron gas of density n. LDA uses only the local density to define the approximate local exchange-correlation potential. This is reasonable as long as $n(\mathbf{r})$ is sufficiently slowly varying.

GGA is another widely adopted functional besides LDA, which accounts for not only the information about the local electron density, $n(\mathbf{r})$, but also the local gradient in the electron density, $\nabla n(\mathbf{r})$

$$E_{\mathrm{XC}}^{\mathrm{GGA}}[n] = \int n(\mathbf{r})\epsilon_{\mathrm{XC}}(n(\mathbf{r}), \nabla n(\mathbf{r}))d\mathbf{r} \tag{1.8}$$

The physical idea of GGA comes from the consideration that electron densities in real materials are not uniform. Because the information from the gradient of the electron density can be included in many ways, a variety of GGA functionals exist, such as the Perdew–Wang functional (PW91),[12] the Perdew–Burke–Ernzerhof functional (PBE),[13] as well as others. In this dissertation, PBE functional with dispersion corrections within the D2 formalism is used for structural relaxation and as mean field starting point for GW and GW-BSE calculations. LDA functional is used for magnetic ground state energy calculations.

1.2 The GW-BSE Method

For excited states, the computational effort becomes extremely large when solving the Hamiltonian of an interacting many-electron system to obtain the many-particle wavefunction. Fortunately, in practice we are interested in excited-state properties such as excitation spectra and expectation values of single-particle operators, which do not require the full knowledge of the wavefunctions and can be obtained from the Green's function. The *ab initio* GW-BSE approach, based on the many-body perturbation theory within the Green's function formalism, can be used to investigate excited-state properties related to one- and two-particle excitations.[14–17] The *ab initio* GW-BSE approach has been implemented in software packages such as BerkeleyGW,[18] ABINIT,[19] yambo,[20] etc.

1.2.1 The GW method

The quasiparticle GW method is based on single-particle Green's function, which only involves one-particle excitation, i.e., the electron addition $(N-1)$ or removal $(N+1)$ process in the N-electron system. The single-particle Green's function is defined (at zero temperature) as

$$G(1,2) = -i\langle N,0\big|T\big[\hat{\psi}(1)\hat{\psi}^{\dagger}(2)\big]\big|N,0\rangle \tag{1.9}$$

where 1 and 2 each stand for the five coordinates of a particle: space ($\mathbf{r}$), spin (ξ) and time (t), e.g., $(1) = (\mathbf{r_1}, \xi_1, t_1) = (\mathbf{x_1}, t_1)$. $|N,0\rangle$ is the exact ground state of the N-electron system. T is the Dyson time-ordering operator which has the effect of ordering the operators with earlier time on the right. $\hat{\psi}$ and $\hat{\psi}^{\dagger}$ are the fermion annihilation and creation operators in the Heisenberg picture. G is closely related to fundamental properties of quasi-electron and quasi-hole. The two-particle Green's function is defined as

$$G_2(1,2;1',2') = -\langle N,0|T[\hat{\psi}(1)\hat{\psi}(2)\hat{\psi}^\dagger(2')\hat{\psi}^\dagger(1')]|N,0\rangle \tag{1.10}$$

which provides information about processes involving two-particle transitions and their interaction through the time ordering of the four times in the equation.

Starting from the Heisenberg equation of motion, one gets the equation of motion for the Green's function

$$\left[i\frac{\partial}{\partial t_1} - H_0(1)\right]G(1,2) - \int \Sigma(1,3)G(3,2)d3 = \delta(1,2) \tag{1.11}$$

where $H_0 = -\frac{1}{2}\nabla^2 + V_{\text{ext}} + V_H$. Σ is the self-energy operator which represents the complicated correlation effects of a many-particle system. With time-translational invariance, Fourier transformation of Eq. (1.11) with respect to $t - t'$ gives

$$[\omega - H_0(\mathbf{x})]G(\mathbf{x},\mathbf{x}';\omega) - \int \Sigma(\mathbf{x},\mathbf{x}'';\omega)G(\mathbf{x}'',\mathbf{x}';\omega)d\mathbf{x}'' = \delta(\mathbf{x},\mathbf{x}') \tag{1.12}$$

which is the Dyson equation that links the interacting single-particle Green's function $G(\mathbf{x},\mathbf{x}';\omega)$ to the non-interacting single-particle Green's function $G_0(\mathbf{x},\mathbf{x}';\omega)$

$$G(\mathbf{x},\mathbf{x}';\omega) = G_0(\mathbf{x},\mathbf{x}';\omega) + \int G_0(\mathbf{x},\mathbf{x_1};\omega)\Sigma(\mathbf{x_1},\mathbf{x_2};\omega)G(\mathbf{x_2},\mathbf{x}';\omega)d\mathbf{x_1}d\mathbf{x_2} \tag{1.13}$$

Here, G_0 can be obtained by mean-field calculations. We note that the self-energy operator Σ is in general nonlocal, non-Hermitian and frequency dependent. A series expansion of Σ in v gives as first term the Hartree-Fock exchange potential. Since both V_H and Σ can be given in terms of G, Eq. (1.12) represents a self-consistency problem that can also be formulated as a variational problem.

One can obtain the Lehmann representation of the single-particle Green's function

$$G(\mathbf{x},\mathbf{x}';\omega) = \sum_s \frac{f_s(\mathbf{x})f_s^*(\mathbf{x}')}{\omega - \epsilon_s + i\eta\,\text{sgn}(\epsilon_s - \mu)} \tag{1.14}$$

in terms of Lehman amplitudes $f_s(\mathbf{x})$ and energies ϵ_s defined by

$$f_s(\mathbf{x}) = \langle N, 0|\hat{\psi}(\mathbf{x})|N+1, s\rangle,\ \epsilon_s = E_{N+1,s} - E_{N,0} \text{ when } \epsilon_s \geq \mu$$
$$f_s(\mathbf{x}) = \langle N-1, 0|\hat{\psi}(\mathbf{x})|N, 0\rangle,\ \epsilon_s = E_{N,0} - E_{N-1,s} \text{ when } \epsilon_s < \mu \quad (1.15)$$

where $\eta = 0^+$ and $\mu = E_{N+1,0} - E_{N,0}$ is the chemical potential. The sum s runs over all states of the $N+1$ and $N-1$ particle systems. Hence, ϵ_s, the poles of G, correspond to electron addition and removal energies. Supposing that Σ is known, by inserting G in terms of $f_s(\mathbf{x})$ and ϵ_s into Eq. (1.12) one finds that for a discrete energy level ϵ_s, the amplitudes $f_s(\mathbf{x})$ and the energies ϵ_s are solutions to the eigenvalue equation

$$[\omega - H_0(\mathbf{x})]f(\mathbf{x}) - \int \Sigma(\mathbf{x}, \mathbf{x}''; \omega) f(\mathbf{x}'') d\mathbf{x}'' = 0 \quad (1.16)$$

The central problem to solve the equation is to develop a good approximation of Σ. Hedin proposed to expand Σ in terms of a screened potential W rather than the bare Coulomb potential v with Schwinger's functional derivative technique, where W is defined as

$$W(1,2) = \int v(1,3)\varepsilon^{-1}(3,2)d3 \quad (1.17)$$

Here, ε is the dielectric matrix and W represents the effective interaction between two particles, which is much weaker than v if the polarizability is large. Considering only the lowest order contributions of the series expansion in W leads to the so-called GW approximation (GWA). Within GWA, the self-energy operator is approximated by[14]

$$\Sigma(1,2) = iG(1,2)W(1^+, 2) \quad (1.18)$$

with the dynamically screened potential W expressed as

$$W(1,2) = v(1,2) + \int v(1,3)P(3,4)W(4,2)d(3,4) \quad (1.19)$$

where $1^+ = \mathbf{x_1}, t_1 + \eta$. Like G, W also satisfies a Dyson-like equation. The kernel P reduces to

$$P(1,2) = -iG(1,2^+)G(2,1) \tag{1.20}$$

where the Fourier transformation of the time-ordered polarization operator P with GWA takes the same form as that deduced from random phase approximation.[21–23] Together with the Dyson equation Eq. (1.13) which links G and Σ, a set of equations that must in principle be solved self-consistently for G is formed.

The time consumption of this method results in a series of approximations applied in the calculations. Within random phase approximation, the interacting polarizability P is replaced by the non-interacting polarizability $P^0(1,2) = -iG_0(1,2^+)G_0(2,1)$, where the non-interacting Green's function G_0 can be constructed from the mean-field eigenstates.[21–23] The simplest GW method, referred to as one-shot GW approach (G_0W_0), calculate the QP self-energy from a nonself-consistent procedure with no iteration by $\Sigma(1,2) = iG_0^{DFT}(1,2)W_0(1^+,2)$. Assuming the wavefunctions from DFT are good approximations for the QP wavefunctions, the QP energies E_{nk} are predicted perturbatively to the lowest order by

$$E_{n\mathbf{k}}^{QP} = E_{n\mathbf{k}}^{DFT} + \langle \psi_{n\mathbf{k}} | \Sigma(E_{n\mathbf{k}}^{DFT}) - V_{\mathrm{XC}} | \psi_{n\mathbf{k}} \rangle \tag{1.21}$$

where E_{nk}^{DFT} is the DFT eigenenergy and V_{XC} is the exchange-correlation potential from DFT calculations. Generally, G_0W_0 leads to quite accurate results for single-particle properties such as the QP energies and the QP lifetime.

1.2.2 The GW-BSE method

For two-particle excitations, the two-particle correlation function L with the inclusion of electron-hole interaction is expressed as[16]

$$L(1,2;1',2') = -G_2(1,2;1',2') + G(1,1')G(2,2') \tag{1.22}$$

The electron-hole correlation function obeys a Dyson equation (known as Bethe–Salpeter equation)

$$L(1,2;1',2') = L_0(1,2;1',2') + \int L_0(1,4;1',3)K(3,5;4,6)L(6,2;5,2')d(3456) \tag{1.23}$$

where $L_0(1,2;1',2') = G(1,2')G(2,1')$ describes the non-interacting quasi-electron and quasi-hole pair. K is the interaction kernel for the two-particle (electron-hole here) excited states.[15,17] Within the GWA, the BSE kernel is found by taking the functional derivative of the self-energy[17,24,25]

$$\begin{aligned} K(3,5;4,6) &= \frac{\delta[V_H(3)\delta(3,4) + \Sigma(3,4)]}{\delta G(6,5)} \\ &= -i\delta(3,4)\delta(5^-,6)v(3,6) + i\delta(3,6)\delta(4,5)W(3^+,4) \end{aligned} \tag{1.24}$$

Here, K consists of two contributions, the exchange kernel (K^x) involving the bare Coulomb interaction, and the direct kernel (K^d) involving the screened Coulomb interaction. Using the QP states ($|cv,\mathbf{k}\rangle = |c,\mathbf{k}\rangle \otimes |v,\mathbf{k}\rangle$) as a basis to expand the exciton (electron-hole pair) state[17]

$$|S\rangle = \sum_{cv,\mathbf{k}} A^S_{cv,\mathbf{k}} |cv,\mathbf{k}\rangle \tag{1.25}$$

the BSE turns into a set of coupled exciton eigenstate and eigenvalue problems

$$A^S_{cv,\mathbf{k}}\left(E_{c,\mathbf{k}} - E_{v,\mathbf{k}}\right) + \sum_{c'v',\mathbf{k}'} A^S_{c'v',\mathbf{k}'} \langle cv,\mathbf{k}|K^{eh}|c'v',\mathbf{k}'\rangle = A^S_{cv,\mathbf{k}}\Omega^S \tag{1.26}$$

where $A^S_{cv,\mathbf{k}}$ is the $\mathbf{k}$-space exciton envelope function, and $|cv,\mathbf{k}\rangle$ corresponds to a free electron-hole pair (i.e., a non-interacting interband transition state) at the point $\mathbf{k}$ of the Brillouin zone. The eigenvalue Ω^S is the excitation energy of an exciton eigenstate $|S\rangle$. Therefore, the first term in Eq. (1.26) corresponds to a non-interacting electron-hole transition, while the second term describes the Coulomb interaction between the non-interacting electron-hole transition in the first term and

all other possible non-interacting electron-hole transitions. These excitons are primarily responsible for the optical absorption and photoluminescence of materials. However, the coupling term between the excited states and external electromagnetic fields are not included in Eq. (1.26). Optical absorption and conductivity are proportional to the imaginary part of the macroscopic dielectric function $\varepsilon_2(\omega)$, which can be constructed from the solution of the BSE[26]

$$\varepsilon_2(\omega) = \frac{8\pi^2 e^2}{\omega^2} \sum_S \left| \hat{\lambda} \cdot \langle 0|\mathbf{v}|S\rangle \right|^2 \delta(\omega - \Omega^S) \tag{1.27}$$

where $\hat{\lambda}$ is the polarization vector, and $\mathbf{v}$ is velocity operator.

The high computational cost in the calculation of various matrix elements and other matrix operations is the main limiting factor of the *ab initio* GW-BSE calculation. As a powerful and accurate method to quantitively evaluate the optical properties of material systems in the linear regime, the *ab initio* GW-BSE approach is still in need of expanding the functions to include dynamical effects and to improve the efficiency for large complex systems.

1.3 Van der Waals Magnetic Semiconductors

Van der Waals materials have emerged as a fertile ground for exploring novel physical phenomena and are highly attractive as a promising class of materials for applications ranging from nanoelectronics and nanophotonics to sensing. One of the most intriguing aspects of vdW materials lies in the ability to manipulate and control their physical properties by precisely adjusting interlayer interactions. This capability has sparked significant interest in the realm of vdW heterostructures and moiré superlattices, leading to remarkable discoveries such as the emergence of strongly correlated phases arising from moiré bands and the formation of interlayer excitons trapped in the moiré potential.[27–31] Within the family of vdW materials, two-dimensional vdW

magnets stand out as they introduce an entirely new magnetic degree of freedom, which opens up unique opportunities for engineering vdW interfaces and developing innovative magnetoelectric, magneto-optic, and spintronic devices.[32,33] In vdW magnets, the interlayer exchange, although considerably weaker compared to the intralayer exchange, plays a crucial role in determining the magnetic order of the entire system.[34] Previous studies have demonstrated that the interlayer magnetic interactions can be fine-tuned using a range of methods including magnetic fields, electric fields, doping, pressure, and stacking.[1,35–42] This extensive tunability paves the way for not only uncovering new magnetic phases, like noncollinear moiré magnetism,[43–45] but also the creation of compact and energy-efficient spintronic devices.

Chapter 2

Optical Transitions in CrSBr Controlled by Interlayer Electronic Coupling

The 2D character of atomically thin layers suggests a strong enhancement of the Coulomb interaction leading to the formation of strongly bound excitons, which dominates the optical and charge-transport properties.[46–48] Compared to bulk materials, the weak yet tunable interlayer coupling adds layer degree of freedom in vdW 2D materials, which enables vdW interfacial engineering for exploration of rich physical phenomena.[49,50] In vdW 2D materials, the optical transitions are controlled by interlayer electronic coupling, which is determined by stacking configurations and external fields.[51–56] In this chapter, we focus on studying the distinct optical properties of 2D magnetic semiconductors controlled by interlayer electronic coupling.

Within the family of vdW magnets, CrSBr is an A-type magnetic semiconductor with direct band gap. The lattice of CrSBr is composed of vdW layers, each formed by two buckled CrS planes terminated by Br atoms (Fig. 2.1a). These layers stack along the *c*-axis, resulting in an orthorhombic structure with P_{mmn} space group. Each CrSBr monolayer is ferromagnetic (FM), but the neighboring layers are antiferromagnetically (AFM) coupled.[57–61] CrSBr exhibits in-plane magnetic anisotropy with easy axis along the *b*-axis, and hard axis along the out-of-plane *c*-axis. The Néel temperature is ~132 K for bulk CrSBr and increases to ~150 K down to the monolayer limit, which is notably higher than that of vdW magnetic semiconductors such as CrX_3 (X=Cl, Br, I) and $Cr_2Ge_2Te_6$.[32,33,62,63] The tunable magnetic and optical properties of CrSBr make it an ideal platform to explore novel physical phenomena.

2.1 Anisotropic Wannier Excitons in CrSBr Monolayers

Electronic structure calculations of monolayer CrSBr in its FM ground state within the GW approximation reveal a semiconducting bandgap of ~1.8 eV and highly anisotropic band dispersion, shown by the spin-polarized GW band structure of monolayer CrSBr in Fig. 2.1b. A large self-energy correction of ~1.3 eV for the bandgap is obtained at the GW level due to strong many-electron effects in 2D. The valence band maximum (VBM) is at the Γ point, and two nearly degenerate conduction band minima (CBM) appear at Γ and X points, with the same spin orientation for CBM and VBM. Despite a different quasiparticle bandgap and dispersion, our GW calculations that include the self-energy corrections are in agreement with previous DFT calculations that also predicted anisotropic and spin-polarized bands.[60,61,64] Away from Γ, there is considerable anisotropy of the conduction bands, with significant dispersion along Γ–Y and almost flat bands along Γ–X. This feature is consistent with the calculated optical matrix element that is dipole-allowed along the *b*-axis, but forbidden along the *a*-axis, for interband transitions from the VBM to the CBM at the Γ point. The first two conduction bands are nearly degenerate at the GW level (labeled CBM1 and CBM2, respectively). The calculated optical matrix element shows the VBM–CBM1 transition is dipole allowed, while the VBM–CBM2 transition is dipole forbidden, which can be understood from the optical selection rules. To illustrate this, we examine the orbital composition of VBM, CBM1 and CBM2 (shown in Fig. 2.1c). Based on the parity and spin of the band extrema, the VBM–CBM1 transition is allowed, but the VBM–CBM2 transition is forbidden. However, by reduction of symmetry (e.g. by an asymmetric dielectric environment), the VBM to CBM2 transition could be brightened.

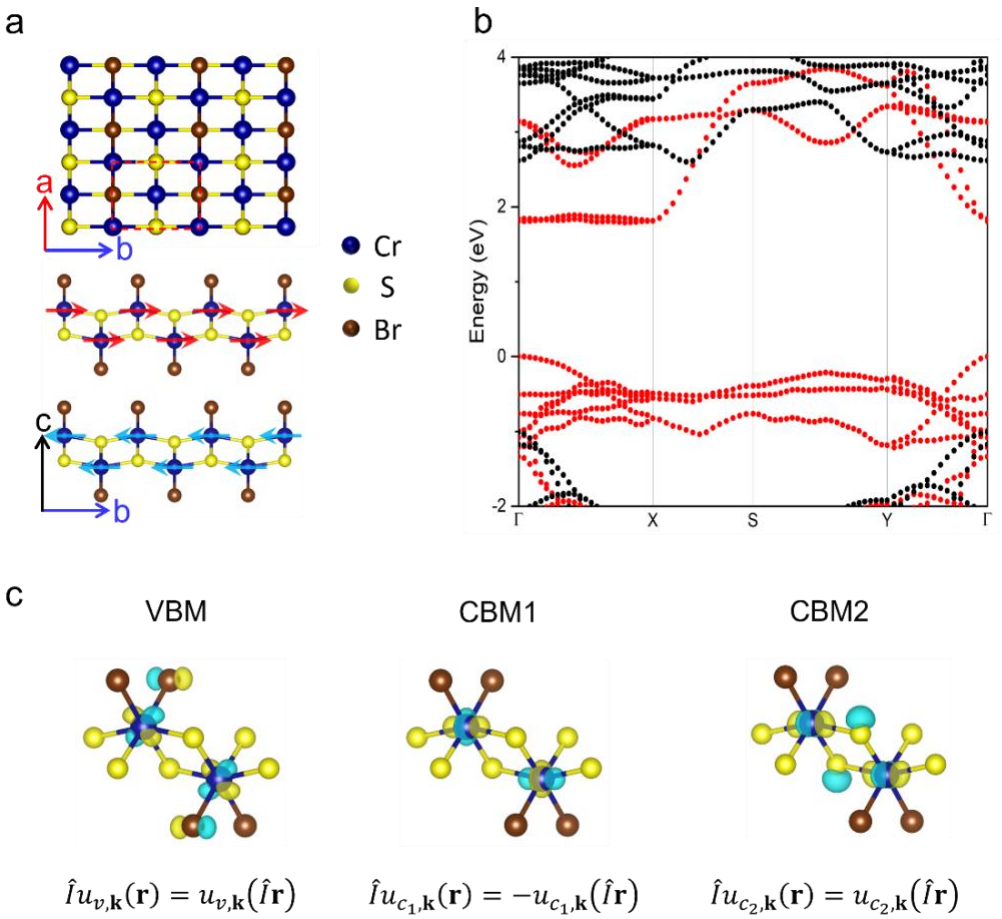

Figure 2.1 Crystal structure and electronic properties of CrSBr. (a) Crystal and magnetic structures of CrSBr. Top image shows a top-view of a single layer and the bottom image shows a side-view of a bilayer in which the AFM order is represented by the red and blue arrows. (b) Calculated quasiparticle band energies using the GW method for monolayer CrSBr. The bands of majority- and minority-spin electrons are shown in red and black, respectively. (c) The orbital composition of VBM, CBM1 and CBM2. The transformation of the wavefunction $u_{i,k}(\mathbf{r})$ under spatial inversion ($\hat{I}$) is noted below each diagram.

The exciton energy levels for monolayer CrSBr obtained from GW-BSE calculations (details in Methods) are shown in Fig. 2.2a. The first two excitons marked by A and B originate from the VBM–CBM1 and VBM–CBM2 transitions, respectively. The calculated optical spectrum for

monolayer CrSBr is shown in Fig. 2.2b. The dominant optical transitions come from bright state A, with the calculated exciton binding energy of ~0.5 eV for a free-standing monolayer. For comparison, the exciton binding energy estimated from a comparison of scanning tunneling spectroscopy and PL spectrum is ~0.25 eV for a bulk crystal.[57] The larger exciton binding energy of the monolayer than that of the bulk is expected from the reduced dielectric screening in the former. The calculated exciton wavefunction (top view in Fig. 2.2c) extends over several unit cells, revealing Wannier character of exciton, distinct from the Frenkel nature of excitons in CrI_3.[65] The calculated exciton wavefunction also shows significant anisotropy, with exciton wavefunction about 2 ~ 3 times more delocalized along the *b* axis than that along the *a* axis, consistent with the effective mass anisotropy along Γ–X and Γ–Y directions obtained from band structures.

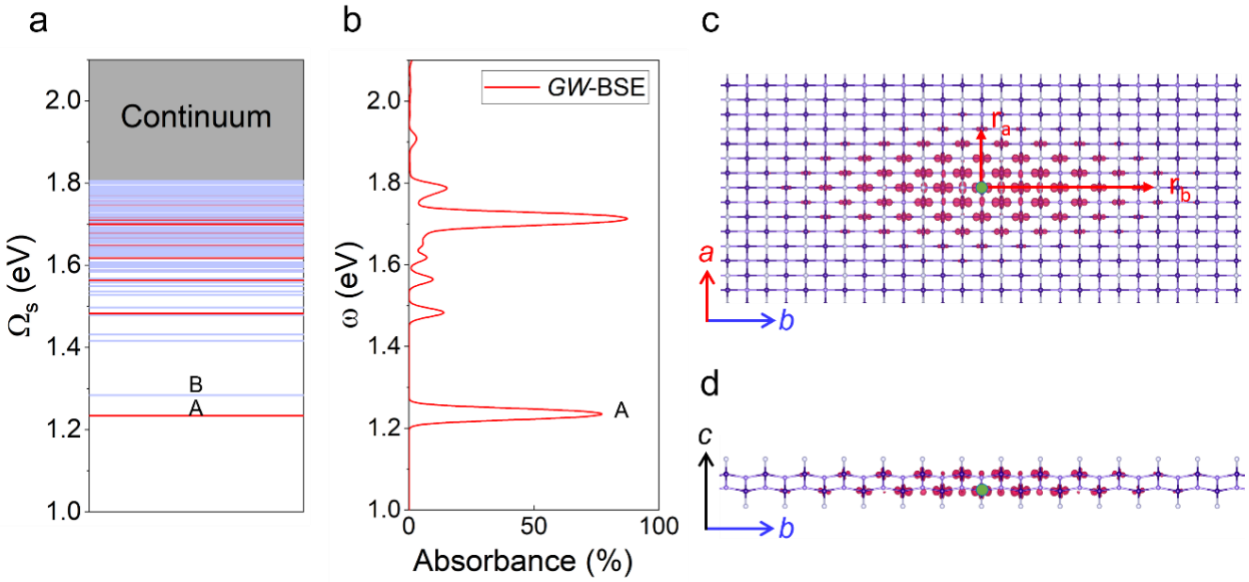

Figure 2.2 Excitonic transitions of monolayer CrSBr. (a) Calculated exciton energy levels obtained from GW-BSE method for monolayer CrSBr. Bright and dark excitons are represented by red and blue lines, respectively. The first two excitons are labeled A (bright) and B (dark). (b) Calculated optical absorption spectra of linearly polarized light (polarization along the *b* axis) of monolayer CrSBr. A Gaussian broadening of 0.01 eV is used to model the imaginary part of the dielectric function. For polarization along the *a* axis, absorbance goes to zero. (c) Top and (d) side views of real-space wavefunction of the lowest-energy exciton, shown as $|\psi_e|^2$ for an electron with the hole fixed near a Cr atom (green circle) in the bottom layer. The iso-surfaces represent $|\psi_e|^2$ set at 1% of its maximum.

2.2 Coupled Exciton Transitions in vdW Layered Magnets

To study the effects of interlayer electronic coupling on optical transitions in layered magnetic semiconductors, we consider layered materials with two neighboring layers labeled by layer 1 and layer 2. For monolayer CrSBr, the lowest-energy optical transition is dipole-allowed. So, we focus on the frontier conduction bands (i.e., $|c_1, \mathbf{k}\rangle$ and $|c_2, \mathbf{k}\rangle$) or valance bands (i.e., $|v_1, \mathbf{k}\rangle$ and $|v_2, \mathbf{k}\rangle$)

in layer 1 and layer 2, schematically shown by the parabolic bands in Fig. 2.3. For vdW semiconductors with weak excitonic interaction (Fig. 2.3a), each pair of valence band and conduction band hosts an exciton series. Therefore, two dipole-allowed transitions and two dipole-forbidden transitions are obtained from the interband optical matrix elements with interlayer wavefunction hybridization, which are consistent with the results for nonmagnetic vdW materials such as black phosphorene.[66] However, if excitonic effects are not negligible, the interband transitions will be coupled by Coulomb interactions and the above interband transition picture will no longer hold. Here we propose a toy model called coupled exciton transition model, where the optical transitions are given by coupled intra- and interlayer excitons (Fig. 2.3b). Choosing the two intralayer excitons ($|X_{11}^s\rangle = \sum_k A_k^S |c_1 v_1, \mathbf{k}\rangle$, $|X_{22}^s\rangle = \sum_k A_k^S |c_2 v_2, \mathbf{k}\rangle$) and two interlayer excitons ($|X_{21}^s\rangle = \sum_k A_k^S |c_2 v_1, \mathbf{k}\rangle$, $|X_{12}^s\rangle = \sum_k A_k^S |c_1 v_2, \mathbf{k}\rangle$) as the basis, we can write the effective Hamiltonian of this toy model as follows

$$H = \begin{pmatrix} 0 & 0 & t_c & t_v \\ 0 & 0 & t_v & t_c \\ t_c & t_v & U & 0 \\ t_v & t_c & 0 & U \end{pmatrix} + E_{\text{intra}}^{1s} I_{4\times 4} \tag{2.1}$$

where the envelope functions A_k^S are assumed to be the same for intra- and interlayer excitons. $t = t_v$ or t_c denotes the interlayer hopping between valence bands or conduction bands. The binding energy U is defined as $U = E_{\text{inter}}^S - E_{\text{intra}}^S$, where E_{inter}^S and E_{intra}^S are eigenvalues for inter- and intralayer excitons.

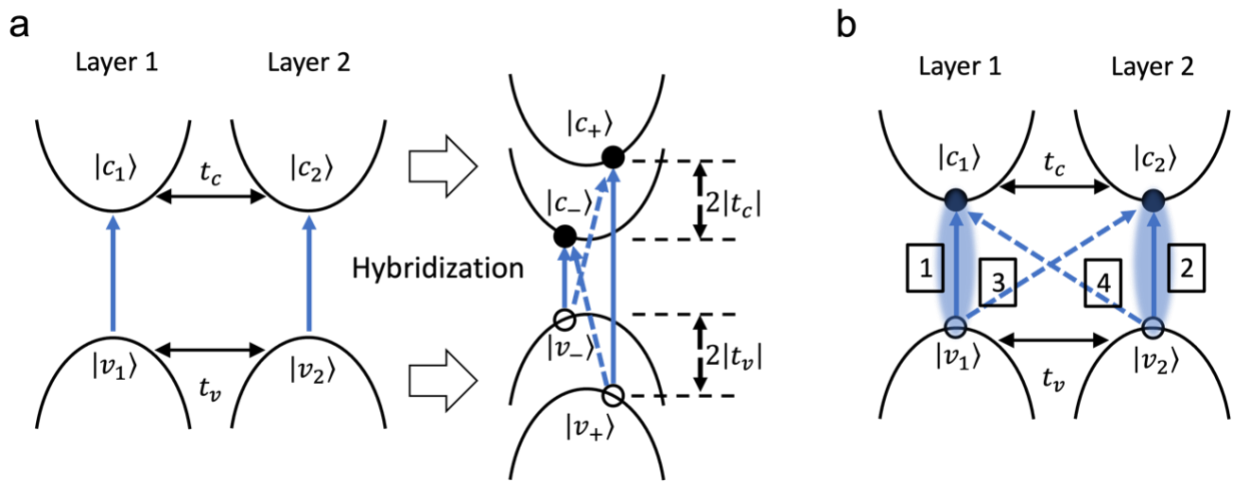

Figure 2.3 Models for optical transitions in 2D layered systems. (a) Schematic for interband optical transitions with weak excitonic interaction. With interlayer wavefunction hybridization between degenerate bands in layer 1 and 2, bonding ($|c_-\rangle$ and $|v_-\rangle$) and anti-bonding ($|c_+\rangle$ and $|v_+\rangle$) states are obtained. The two solid lines represent the dipole-allowed $|v_+\rangle$ to $|c_+\rangle$ and $|v_-\rangle$ to $|c_-\rangle$ transitions, while the two dashed lines represent the dipole-forbidden $|v_-\rangle$ to $|c_+\rangle$ and $|v_+\rangle$ to $|c_-\rangle$ transitions. (b) Schematic for coupled exciton transition model with strong excitonic interaction. The two intralayer excitons are labeled by exciton 1 (state $|X_{11}^s\rangle$) and exciton 2 (state $|X_{22}^s\rangle$), while the two interlayer excitons are labeled by exciton 3 (state $|X_{21}^s\rangle$) and exciton 4 (state $|X_{12}^s\rangle$). The intra- and interlayer excitons are coupled by Coulomb interactions.

By diagonalizing the Hamiltonian in Eq. (2.1), we get the exciton energies relative to the eigenvalues of 1s intralayer excitons, in the order of energy from low to high under our assumption that $t_c > 0$ and $t_v < 0$

$$E_1 = \frac{U}{2} - \sqrt{(t_c - t_v)^2 + \left(\frac{U}{2}\right)^2}, E_2 = \frac{U}{2} - \sqrt{(t_c + t_v)^2 + \left(\frac{U}{2}\right)^2},$$
$$E_3 = \frac{U}{2} + \sqrt{(t_c + t_v)^2 + \left(\frac{U}{2}\right)^2}, E_4 = \frac{U}{2} + \sqrt{(t_c - t_v)^2 + \left(\frac{U}{2}\right)^2} \quad (2.2)$$

And the optical transition matrix elements can be obtained by

$$\langle 0|\boldsymbol{p}|S\rangle = \sum_{\mathbf{k}}^{\mathrm{h}} \sum_{v} \sum_{c}^{\mathrm{e}} A^{S}_{vc\mathbf{k}} \langle v_{\mathbf{k}}|\boldsymbol{p}|c_{\mathbf{k}}\rangle \quad (2.3)$$

As a result, we obtain entangled electron-hole states between layers for the eigenstates, with only one bright excitonic transition with E_2 in the coupled exciton transition picture under the limit of $t \ll U$ (shown in Fig. 2.4b). Besides, in contrast to the linear dependence of E on t with weak excitonic effects ($t \gg U$), the relative exciton energies in the coupled exciton transition picture show that $E \propto t^2$ due to coupled inter- and intralayer excitons under the limit of $t \ll U$, as demonstrated by the example of simulations depicted in Fig. 2.4a. Next, we will investigate our model by examining the effects of interlayer electronic coupling on optical transitions in CrSBr bilayers.

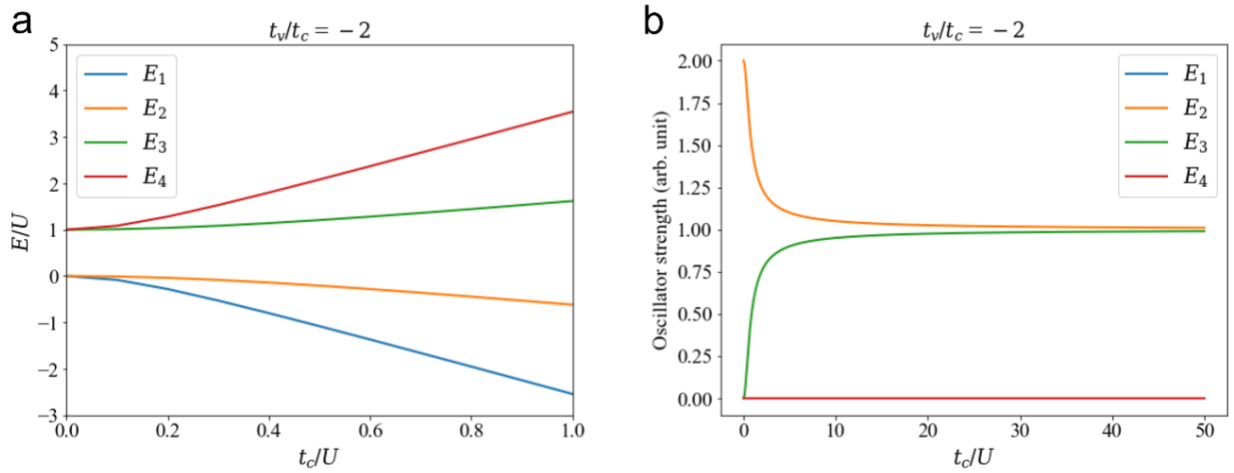

Figure 2.4 Simulations for relative exciton energies and corresponding oscillator strengths of optical transitions in the coupled exciton transition model. (a) Assuming $t_v/t_c = -2$, the simulated results for the dependence of exciton energies E/U on the interlayer hopping term t_c/U, where E^{1s}_{intra} is set to 0. (b) Assuming $t_v/t_c = -2$, the simulated results for the dependence of oscillator strengths on the interlayer hopping term t_c/U for the optical transitions. The oscillator strengths are normalized to the values at the $t \gg U$ limit.

2.3 Magneto-Excitonic Coupling in CrSBr Bilayers

The quasiparticle band structures of bilayer CrSBr in the AFM (Fig. 2.5a) and FM (Fig. 2.5b) states are obtained from first-principles GW calculations (details in Methods). In the AFM bilayer, the product symmetry of time reversal and spatial inversion makes the band structure degenerate in spins. In each Bloch band near the doubly degenerate CBM and VBM, the spin-up or spin-down electrons are localized at the top and bottom layer, respectively, since their interlayer hybridization is suppressed by the interlayer AFM order. In the FM bilayer, by contrast, the electrons in the two layers can resonantly couple with each other, leading to band splitting of the CBM and VBM and a band gap reduction of ~0.1 eV relative to the AFM bilayer. The GW-BSE calculations unveil the

nature of optical transitions. The dominant optical transitions arise from the lowest-energy exciton in CrSBr bilayers, with the calculated exciton binding energies of ~0.46 eV and ~0.37 eV for free-standing AFM and FM bilayers, respectively. In the AFM bilayer, the bright excitons in the top and bottom layers are virtually decoupled due to the anti-aligned spins between layers. The lowest energy bright excitons are two-fold degenerate (with energy difference < 0.5 meV), and account for the optical transitions at ~1.34 eV in the experimental spectra. In the FM bilayer, only one bright exciton is obtained with the interlayer electronic coupling turned on by the interlayer FM order and the excitonic effect not negligible, which is consistent with the coupled exciton transition picture we proposed. A comparison between the experimentally measured transition energy and the calculated exciton excitation energy (~1.23 eV) shows a ~0.1 eV difference, which arises from the error of GW-BSE calculations (details in Methods).

The sideview of the exciton wavefunction in Fig. 2.5d confirms that the electron is localized in the same layer as the hole. In the FM bilayer, by contrast, the bright excitons in the two layers are no longer decoupled states due to the interlayer hybridization of the electron and hole orbitals. For the lowest-energy exciton in the FM bilayer, when the hole is fixed in one layer, the associated electron shows significant amplitude in both layers (shown in Fig. 2.5e with a typical side view).

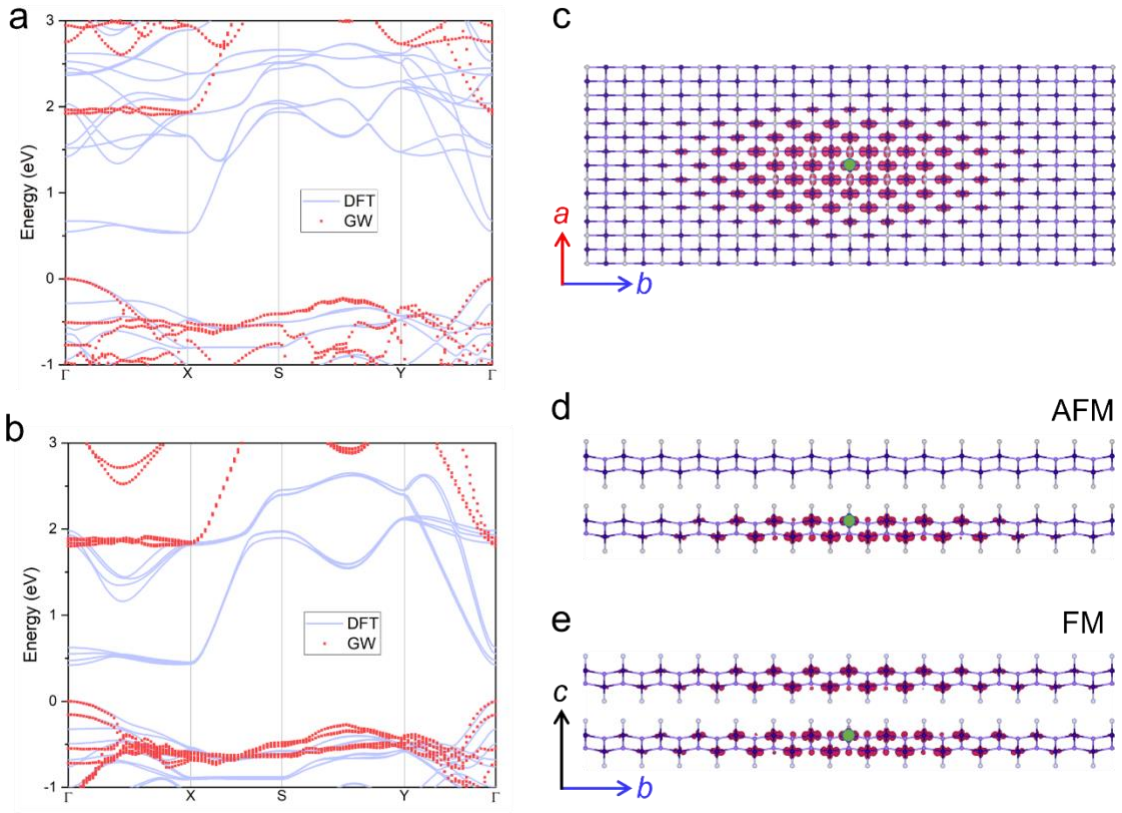

Figure 2.5 Magnetic order-dependent band structures and exciton wavefunctions. Band structures of the (a) AFM and (b) FM CrSBr bilayers. Blue and red dots are Kohn–Sham band energies calculated using the DFT-PBE method and quasiparticle band energies calculated using the GW method, respectively. In the AFM bilayer, bands are degenerate in spin. In the FM case, the bands of majority spins are shown (those of minority spins have much larger gaps). (c)-(e) Real-space wavefunction of the lowest-energy exciton, shown as $|\psi_e|^2$ for an electron with the hole fixed near a Cr atom (green circle) in the bottom layer. The iso-surfaces represent $|\psi_e|^2$ set at 1% of its maximum. (c) Top view in the AFM bilayer. Top view in the FM bilayer is very similar. (d) The side view in the AFM bilayer showing that the electron is virtually localized in the same layer as the hole. (e) The side view in the FM bilayer showing that the electron wavefunction is delocalized across both layers for a hole (green circle) fixed in the bottom layer.

We further quantify interlayer spatial distribution of the exciton wavefunction. The exciton wavefunction of a selected excited state $|S\rangle$ can be casted into

$$\Psi^S(\mathbf{r}_e, \mathbf{r}_h) = \sum_{cv\mathbf{k}} A^S_{cv\mathbf{k}} \psi_{c\mathbf{k}}(\mathbf{r}_e) \psi^*_{v\mathbf{k}}(\mathbf{r}_h) \tag{2.4}$$

with the hole coordinate $\mathbf{r}_h$ fixed at certain point of the bottom layer, while the electron coordinate $\mathbf{r}_e$ running over a real-space mesh in the supercell. $A^S_{cv\mathbf{k}}$ describes the *k*-space exciton envelope function for the exciton state $|S\rangle$ in the quasiparticle state representation. c, v and $\mathbf{k}$ are the conduction-band, valence-band, and *k*-point indices, respectively. To characterize the spatial distributions of exciton wavefunction with hole fixed in all possible spots in the bottom layer, the integral of the wavefunction module square $\rho^S(\mathbf{r}_e)$ is evaluated by

$$\rho^S(\mathbf{r}_e) = \int_{\mathbf{r}_h \in B} \Psi^S(\mathbf{r}_e, \mathbf{r}_h) \Psi^{S*}(\mathbf{r}_e, \mathbf{r}_h) d\mathbf{r}_h \tag{2.5}$$

where $\mathbf{r}_h$ runs over the bottom layer as the location of the hole may result in different electron wavefunction distributions in the FM bilayer. As $\int_{\mathbf{r}_h \in B} \psi^*_{v\mathbf{k}}(\mathbf{r}_h) \psi_{v'\mathbf{k}'}(\mathbf{r}_h) d\mathbf{r}_h = 0, \forall \mathbf{k} \neq \mathbf{k}'$ for two-dimensional materials, $\rho^S(\mathbf{r}_e)$ may be rewritten as

$$\rho^S(\mathbf{r}_e) = \sum_{cvc'v'\mathbf{k}} A^S_{cv\mathbf{k}} A^{S*}_{cv\mathbf{k}} \psi_{c\mathbf{k}}(\mathbf{r}_e) \psi^*_{c'\mathbf{k}}(\mathbf{r}_e) \int_{\mathbf{r}_h \in B} \psi^*_{v\mathbf{k}}(\mathbf{r}_h) \psi_{v'\mathbf{k}}(\mathbf{r}_h) d\mathbf{r}_h \tag{2.6}$$

which can be obtained from GW-BSE calculations. Therefore, the ratio η^S of the sum of $\rho^S(\mathbf{r}_e)$ in the top layer to that in the bottom layer is used to characterize the layer-resolved spatial distributions of exciton wavefunction

$$\eta^S = \frac{\int_{\mathbf{r}_e \in T} \rho^S(\mathbf{r}_e) d\mathbf{r}_e}{\int_{\mathbf{r}_e \in B} \rho^S(\mathbf{r}_e) d\mathbf{r}_e} \tag{2.7}$$

where $\mathbf{r}_e$ runs over the top and bottom layers, respectively. Here the bottom layer refers to the bottom half of the supercell and the top layer refers to the top half of the supercell. The calculated

η^S is < 0.51% in the AFM bilayer and ~50% in the FM bilayer. In other words, the probability density to find the bound electron in the layer different from that of the fixed hole is > 50 times larger in the FM state than the AFM state, which confirms that the electron is localized in the same layer as the hole in the AFM bilayer and can delocalize over both layers in the FM bilayer.

The calculated optical spectra in the AFM and FM states are shown in Fig. 2.6a. By turning on the interlayer electronic coupling in the FM state, the most visible effect is a redshift of the optically bright exciton by ~10 meV from that in the AFM state. This calculated redshift is consistent with the experimental measurements, as shown by the differential reflectance spectra from bilayer CrSBr in the AFM (blue) and field-induced FM (red) states, respectively (Fig. 2.6b). Another noteworthy observation in the absorption spectra is the presence of a minor peak (marked by B) on the higher-energy side of the predominant peak (marked by A). This peak is attributed to the originally dark B exciton at the monolayer limit acquiring a small dipole due to symmetry breaking.

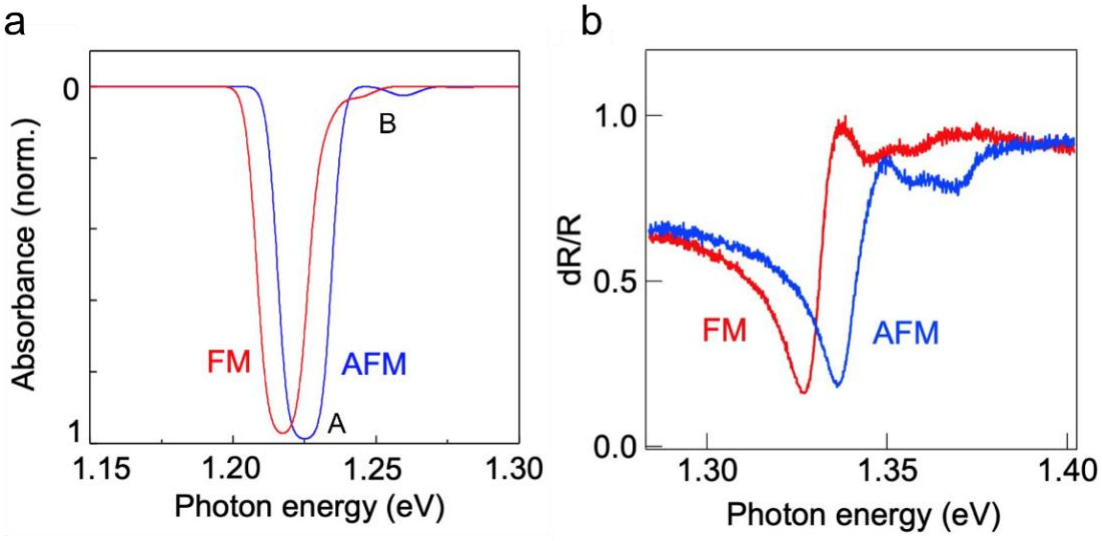

Figure 2.6 Calculated and measured optical spectra of monolayer CrSBr. (a) Calculated optical absorption spectra of linearly polarized light (polarization along the *b* axis) of the AFM (blue) and FM (red) CrSBr bilayers. A Gaussian broadening of 0.005 eV is used. For polarization along the *a* axis, absorbance goes to zero. The two spectra are normalized to the peak absorbance in the AFM state. (b) Experimentally measured differential reflectance spectra of the AFM (blue) and FM (red) CrSBr bilayers.

The measured photoluminescence (PL) as a function of applied magnetic field (B) along different axes at 5 K is shown in Fig. 2.7 for bilayer CrSBr. As we demonstrated above, the observed magneto-excitonic coupling originated from interlayer electronic interaction. When B is swept along the easy axis, the PL redshifts and intensifies abruptly above a critical field $B_c = 0.134 \pm 0.003$ T and is otherwise constant above and below this transition (Fig. 2.7a). This abrupt switch comes from a spin flip AFM–FM transition, resulting in a sudden transformation of the electronic structure and excitonic transitions. Field sweeps along the intermediate and hard axes result in a continuous evolution of the PL spectrum up to saturation fields B_{sat} of roughly 0.9 and 1.6 T, respectively, beyond which the PL spectrum remains unchanged (Fig. 2.7b, c). This continuous

evolution arises from spin-canting process, which produces continuous evolution of the electronic structure. The interlayer hybridization explains the stark difference between the discrete switching behavior of the excitonic transitions when the magnetic field is along the easy axis and the continuous evolution when it is along the intermediate/hard axis. The wavefunctions near the VBM or CBM of each CrSBr layer can be approximated by the product of the spatial and the spinor parts, with the spatial part nearly independent of the spin orientation. The interlayer hopping integral t is therefore proportional to the inner product of the spinor wavefunctions of adjacent layers, $t \propto \langle S_1 | S_2 \rangle = \cos(\theta/2)$, where θ is the angle between the magnetization vectors of the layers. For the spin flip transition, θ jumps from π to 0 at B_c, while for the spin canting behavior, $M = M_{\mathrm{sat}} \cos(\theta/2) \propto B$ up to B_{sat}. When B is along the intermediate axis, lowest-order energy shift in the perturbation theory gives, $\Delta E \propto t^2 \propto B^2$, as is confirmed in Fig. 2.7d. Moreover, the interlayer hybridization across the vdW interface makes relaxation into the lowest energy bright exciton more efficient and, thus, more competitive with non-radiative recombination. This explains the abrupt increase in PL intensity across the spin flip transition (Fig 2.7a) and the gradual increase in PL intensity as the spins are progressively canted away from the easy axis (Fig. 2.7b, c).

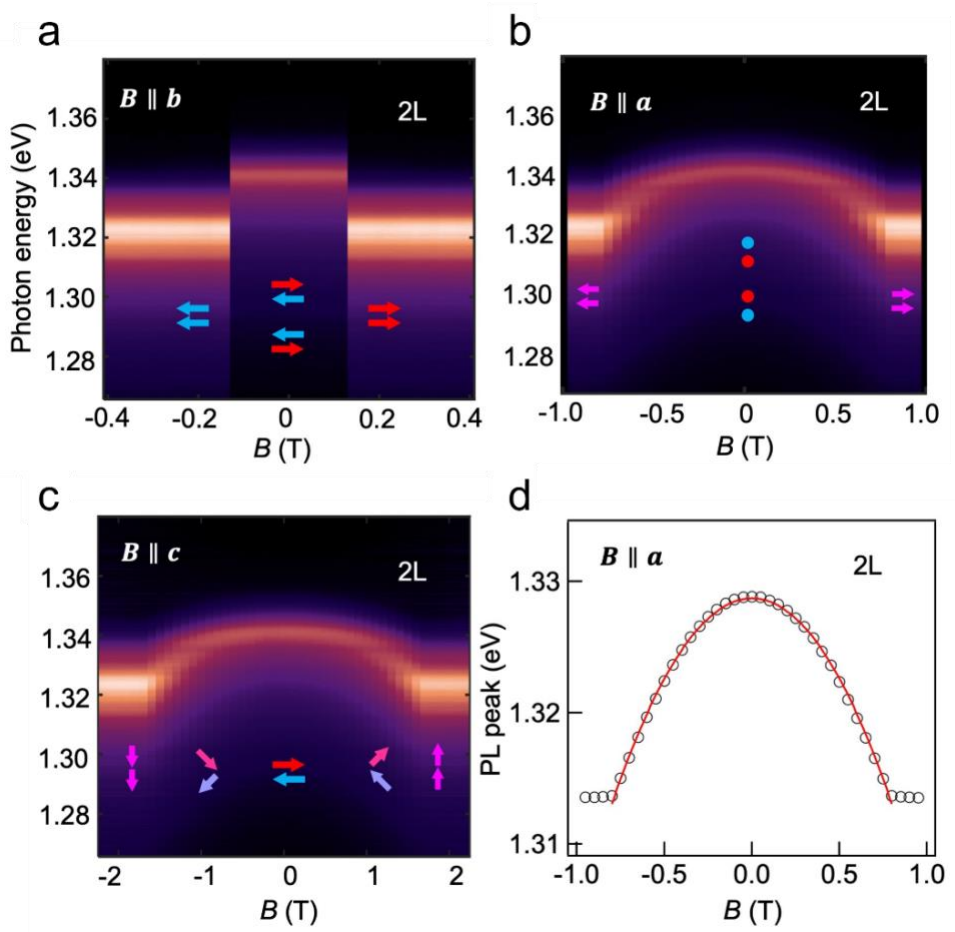

Figure 2.7 Magnetic field dependence of bilayer PL spectrum along the (a) easy, (b) intermediate and (c) hard axes, respectively. In all PL spectra, the polarization of emitted light was along the *b* axis. Colored arrows show the possible orientation of magnetization in both layers (dots represent arrows pointing off the page). (d) Field-dependent PL peak position (center-of-mass, circles) for bilayer CrSBr as a function of magnetic field (B) along the *a* axis. The red curve shows the quadratic fit to experimental data below the saturation field.

2.4 Conclusions

In summary, we find CrSBr as a direct band gap semiconductor with layered A-type AFM order through first-principles DFT calculations and GW-BSE method. The anisotropic Wannier nature

is revealed for the excitonic transitions in CrSBr, which is sensitive to interlayer electronic coupling. Our study finds significant excitonic effects when considering the optical transitions in few-layer CrSBr, with only one bright exciton in the FM CrSBr bilayer. Notably, we demonstrate that excitonic transitions in layered CrSBr can be modified drastically by the interlayer electronic coupling controlled by the magnetic order in layered CrSBr. Therefore, we prove an effective approach to tailor interlayer electronic coupling in vdW semiconductors by control of their magnetic order, and this magneto-electronic coupling opens up possibility of employing simple optical methods to probe or manipulate spin information.

2.5 Computational Methods

The mean-field starting point of the GW calculations uses DFT within the spin-polarized GGA, performed using the Quantum ESPRESSO package.[8] We employed norm-conserving pseudopotentials, with a plane-wave energy cutoff of 85 Ry.[67] In the structural relaxation, we included dispersion corrections within the D2 formalism to account for the vdW interactions.[68] The structure was fully relaxed until the force on each atom was smaller than 0.01 eV/Å. The calculated lattice constants along the a and b axes are 3.511 Å and 4.712 Å, respectively, in agreement with experimental results.[57] The calculated interlayer distance is 8.090 Å in bilayer. The scalar-relativistic and full-relativistic band structures show little differences near the VBM or CBM. The GW[15] calculations were carried out using the BerkeleyGW package[18] at the G_0W_0 level. The supercell in the monolayer and bilayer calculations uses out-of-plane lattice constants of 16 Å and 28 Å. A truncated Coulomb interaction is employed along the out-of-plane direction to avoid interactions between the free-standing CrSBr layers and its periodic images. In the calculation of the electron self-energy, the dielectric matrix was constructed with a cutoff energy of 35 Ry. The

dielectric matrix and the self-energy were calculated on an 8×6×1 k-grid. 10 subsampling points along the in-plane diagonal of the supercell are included in the calculation of the dielectric function.[69] A static remainder approach is used, together with 1,700 bands in the bilayer calculation.[70] These parameters lead to a converged quasiparticle bandgap within 0.1 eV. The exciton energy levels and wavefunctions are calculated using the GW-BSE methods.[17] The exciton interaction kernel is calculated on a 32×24×1 k-grid in bilayer, which converges the exciton binding energy to within 0.1 eV, similar to a previous report on CrI_3.[65]

Chapter 3

Tuning Magnetic Properties of CrSBr by Mechanical Methods

The recent discovery of atomically thin vdW magnets provides an exciting platform for manipulating and tuning magnetic properties at the atomic scale with versatile methods.[50,71] For example, hydrostatic pressure has been used to switch AFM to FM state in the A-type antiferromagnet CrI_3 at zero magnetic field.[41,72] However, the pressure-induced magnetic state transition in CrI_3 is non-reversible, as it originates from the rearrangement of layer stacking from monoclinic to rhombohedral. Consequently, there is a growing demand for the development of a continuously tunable knob as well as the discovery of a suitable material system for achieving reversible magnetic phase transitions. In this chapter, we demonstrate the continuous tuning of the magnetic properties of the vdW magnet CrSBr via uniaxial strain and hydrostatic pressure. These mechanical methods directly modify the lattice constants and symmetry of the crystal, affording dynamic and reversible means of controlling the magnetic behavior of vdW magnets.

3.1 Magnetic Phase Transition Induced by Uniaxial Strain

We calculate the magnetic ground state of bulk CrSBr with uniaxial strain applied along the intermediate a axis (Fig. 3.1a). Without strain applied, the difference between the total energy of FM state and AFM state ($\Delta E = E_{\mathrm{FM}} - E_{\mathrm{AFM}}$) is positive, indicating an AFM ground state for freestanding CrSBr layers. The sign switching from positive to negative as strain increases indicates a strain-induced AFM to FM transition, with a critical strain of ~0.5% along the a axis. We find that the calculated ΔE shows little difference between fixed- and free-boundary

conditions, which correspond to the lattice constants in *b* and *c* kept constant or free to relax. In the latter case, the change in lattice constant *b* and *c* in bulk CrSBr are -0.1% and -0.4%, respectively, for a 1% strain along *a*. We further calculate the dependence of ΔE on strain applied along the *c* axis with lattice constants in *a* and *b* kept constant. CrSBr stays in the AFM phase within ± 2% strain, which suggests that the sign switching of the interlayer magnetic exchange interaction is not a result of changes to the interlayer spacing caused by the Poisson effect. The above results are consistent with strain-dependent PL experiments (Fig. 3.1d). In the absence of a magnetic field, the exciton PL peaks remain nearly unchanged as the strain increases from 0.7% to about 1.1%, which agrees with the first-principles calculations that suggest that a tensile strain of <1% only results in a continuous change of <5 meV of the bandgap in the AFM phase (Fig. 3.1c). As the strain increases to above ~1.1%, the intensity of these peaks decreases, and a new set of peaks emerge. The new features dominate the spectrum above ~1.3%, and remain nearly unchanged as the strain increases further. This energy shift of PL peaks corresponds to an AFM to FM magnetic phase transition, as demonstrated in Chapter 2.

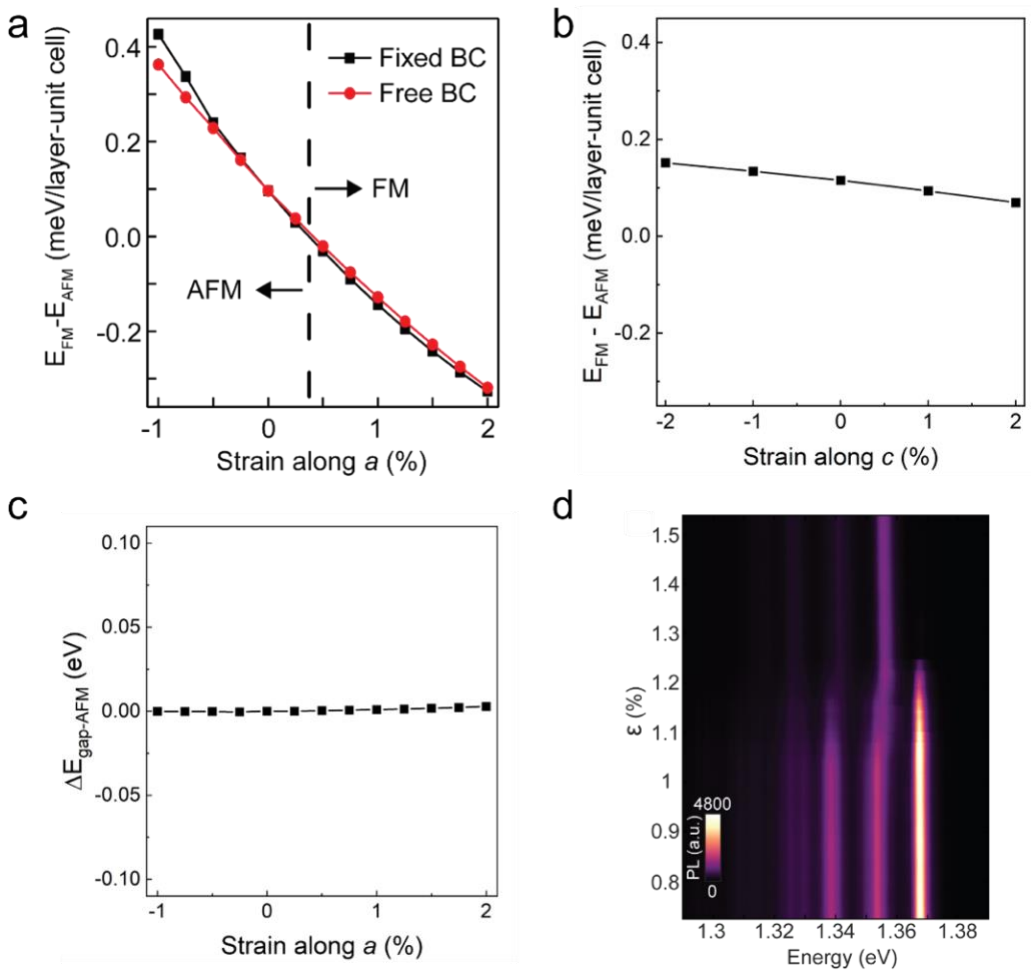

Figure 3.1 DFT and experimental results of strain effects on interlayer magnetic ordering. (a) Calculated energy difference ΔE between the interlayer FM and AFM states as a function of strain applied along the *a* axis. The sign switching from positive to negative is denoted by the dashed black line. Results calculated with fixed and free boundary conditions are denoted by black and red, respectively. (b) Calculated energy difference of FM and AFM interlayer coupling as a function of strain applied along the *c* axis with lattice constants in *a* and *b* kept constant. (c) Calculated change of the band gap, $\Delta E_{\mathrm{gap-AFM}}$, of bulk CrSBr in the interlayer AFM phase as the strain is applied along the *a* axis with free boundary condition. $\Delta E_{\mathrm{gap-AFM}}$ is < 5 meV for strain within ±1%. (d) Strain-dependent PL intensity plot of a 20 nm CrSBr flake with the strain applied along the *a* axis. The strain is swept up from a starting value of ~0.7%.

To understand the origin of the tunability of interlayer magnetic coupling in CrSBr bulk crystals, we calculate the interlayer magnetic exchange interactions by DFT using a four-states mapping analysis.[73] Without strain, we find that the 4th nearest neighbor (NN) interlayer Cr–Cr exchange interactions is needed to correctly describe the antiferromagnetic interlayer coupling. Table **3.1** summarizes the calculated Heisenberg exchange coupling constants J_1, J_2, J_3 and J_4 for the 1st, 2nd, 3rd, and 4th NN interlayer interactions (marked in Fig. 3.2a), together with the total interlayer magnetic coupling per unit cell per interface (E_{inter}) obtained based on J for both 0% and 1.75% strain along the *a* axis. With 1.75% strain applied along the *a* axis, the interlayer magnetic coupling transits from positive to negative, corresponding to the interlayer AFM to FM transition with a certain amount of strain applied, consistent with our previous experimental and theoretical discoveries. We note that E_{inter} obtained from summing over J up to the 4th NN may defer from the exact calculated E_{inter} from DFT, due to factors such as the longer-range interlayer exchange and the magnetic couplings beyond the Heisenberg two-body form, which were not included in the former analysis. However, the trend we observed is robust, i.e., the application of strain reduces the AFM coupling terms and enhances the FM terms. In particular, the change of the ferromagnetic term J_1 is most significant and dominates the AFM-to-FM transition. As a result, it is critical to investigate how the applied strain modifies the Br–Br distances and the Cr–Br–Br angles that decide the magnetic exchange pathway of J_1.

Table 3.1 The calculated Heisenberg exchange coupling constants *J*. Calculated J_1, J_2, J_3 and J_4 for the 1st, 2nd, 3rd, and 4th nearest neighbor interlayer interactions and the total interlayer magnetic coupling per unit cell per interface (E_{inter}) from summing over pairs of *J*. Positive and negative values correspond to the AFM and FM coupling, respectively.

(meV)	J_1	J_2	J_3	J_4	E_{inter}
No strain	-0.0114	0.0063	-0.0025	0.0296	0.170
1.75% strain along a	-0.0238	0.0054	-0.0056	0.0264	-0.003

In Fig. 3.2b, we show the two shortest interlayer magnetic exchange pathways between the closest Cr–Cr pairs in adjacent layers. These two pathways are mediated by two Br ligand *p* orbitals, which are super-super exchange interactions between the two high-spin Cr ions. We next generalize the Goodenough–Kanamori–Anderson rules to study the two pathways.[74–76] Two types of Cr–Br–Br bonds are involved in the Cr–Br–Br–Cr paths. They have bond angles of 97.5° and 140.9° from first-principles calculations, but equal in distance. Although these angles are neither 90° nor 180°, the trend upon changing the angles can be obtained within qualitative analysis. The Cr–Br–Br bond angle close to 90° dictates that two nearly orthogonal Br *p* orbitals (of the middle Br) are involved in the hopping process, and the exchange is mediated by the weak Hubbard on-site interaction among the middle Br *p* orbitals (Hund's rule). Direct *d-p-p* hopping, which has stronger strength, plays more important roles as the bond angle departs from 90°. The 140.9° Cr–Br–Br bond angle allows for *d-p-p* hopping from partially occupied *d* orbitals of Cr to a *p* orbital of the middle Br, then to another collinear *p* orbital of the next Br. Comparing the two bond angles, the Cr–Br–Br path with a 140.9° angle should be stronger since it arises mainly from direct hopping rather than the weak Hubbard type onsite interaction. In Fig. 3.2c, the bond angles in the first pathway between Cr–Br–Br and Br–Br–Cr are both 97.5°, whereas in the second pathway, the

bond angles are 97.5° and 140.9° (Fig. 3.2d), respectively. As such, the second pathway (P2) should dominate the magnetic exchange between the closest interlayer Cr–Cr pairs.

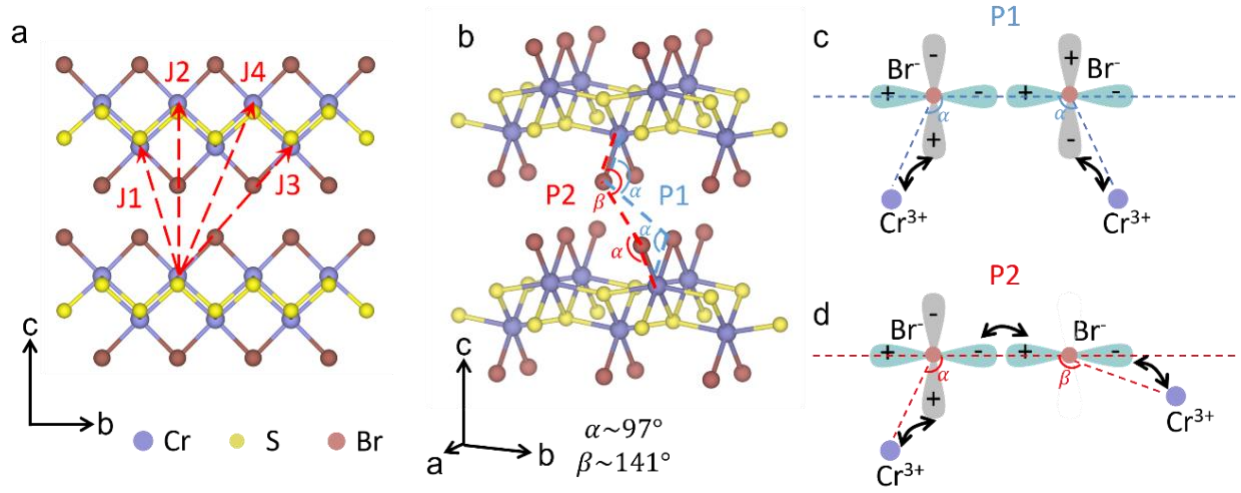

Figure 3.2 Schematics of the interlayer exchange pathways in bulk CrSBr. (a) The interlayer magnetic exchange coupling J_1, J_2, J_3 and J_4 for the 1st, 2nd, 3rd, and 4th NN interlayer Cr pairs. (b) Two interlayer magnetic exchange pathways between closest Cr–Cr interlayer pairs in side view. (c) Schematics of the first exchange pathway, giving weak magnetic exchange coupling. (d) Schematics of the second exchange pathway that favors AFM and FM coupling when α deviates from (compressive strain along a) and approaches (tensile strain along a) 90°, respectively.

We then study how P2 changes with strain. Uniaxial strain applied along the a axis increases the a lattice constant and elongates the Cr–Br bond projected on a. As a result, the Cr–Br–Br bond angle at 97.5° decreases to 96.8° at 1% strain and 96.2° at 2% strain from our first-principles calculations. In contrast, the Cr–Br–Br bond at 140.9° remains virtually unchanged (within 0.1°) due to the particular geometry of the lattice. The Br–Br distance remains unchanged as well (with free boundary conditions in first-principles calculations). As a result, the magnetic super-super exchange of this pathway, consisting of *d-p-p* hopping and Hund's coupling in Br p, becomes more

ferromagnetic as the smaller bond angle approaches 90°, in agreement with the results from first-principles calculations of J_1. In the limit of that the bond angle ~90°, the majority-spin *d* electrons of Cr hops to the *p* orbitals of the first and second Br, then couples ferromagnetically by Hund's rule to an orthogonal *p* orbital (with 90° rotation) of the second Br, and eventually hops to the Cr in the adjacent layer. In conclusion, the couplings between the closest interlayer Cr–Cr pairs favor ferromagnetic super-super exchange interactions, which can be significantly enhanced by moving the Cr–Br–Br bond angle closer to 90° when the in-plane strain applied along the *a* axis. This could be the main mechanism for the strain induced AFM-FM magnetic phase transition.

3.2 Designing Magnetic Properties in 2D Layered Magnets through Hydrostatic Pressure

From Section 3.1, the magnitude and sign of magnetic exchange in CrSBr are highly sensitive to Cr–halogen–Cr and Cr–chalcogen–Cr bond angles. We then chose hydrostatic pressure (P) as the tuning knob to modify the magnetic properties of CrSBr through modifying the structure without changing chemical properties. The primary magnetic couplings consist of three intralayer FM superexchange interactions (denoted J_1, J_2, and J_3) mediated by intralayer Cr–S–Cr and Cr–Br–Cr bonds (Fig. 3.3a, b). The interlayer AFM super-superexchange coupling (J_{inter}) is mediated by Cr–Br–Br–Cr interactions between the sheets. The strong intralayer coupling gives rise to short-range FM correlations below a characteristic temperature T_C~160 K,[57,58] while the weaker interlayer exchange induces long-range A-type AFM order below T_N~132 K.[77] Under hydrostatic pressure, all lattice constants are compressed, with the most significant change along the *c*-axis (Fig. 3.3c).

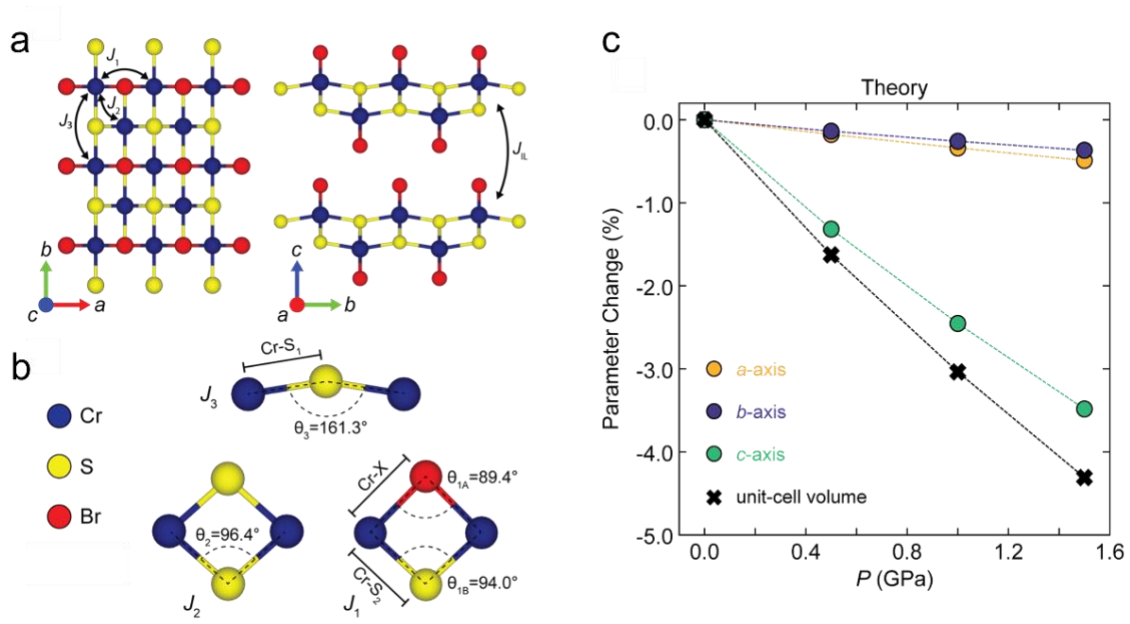

Figure 3.3 Schematic of magnetic couplings and the crystal structures under pressure for bulk CrSBr. (a) Top (left) and side (right) views of crystal structure for bulk CrSBr. Double-ended black arrows denote the direction of the relevant magnetic couplings. (b) Schematic of the superexchange pathways for the three largest intraplanar FM couplings in CrSBr. The corresponding bonds and bond angles contributing to the superexchange interactions are labeled. (c) Calculated percentage change in lattice constants (orange, purple, and green dots for *a*-, *b*-, and *c*-axes, respectively) and the unit-cell volume (black crosses) versus P.

With the structural changes in mind, we further explore the change of intra- and interlayer magnetic exchange couplings under pressure. We find that all primary intralayer FM couplings weaken (Fig. 3.4a) and the magnitude of the strongest intralayer coupling, J_2, is more than 30 times that of J_{inter} for the entire P range, indicating that the intralayer magnetic exchange is the dominant contribution to the ordering temperature. The calculations predict a decreasing T_C with increasing P (Fig.3.4b), which comes from suppressed intralayer FM superexchange interactions, highlighting the delicate balance between Cr–Cr direct exchange and Cr–anion superexchange

pathways (see below). Besides, the interlayer AFM coupling drastically strengthens (inset of Fig. 3.4a) as the *c*-axis compresses. The increase of J_{inter} can be explained by the increase of Cr–Br–Br–Cr overlap, resulting from the significant decrease of the theoretically predicted vdW gap (~10% at 1.5 GPa) with P, and this explains the increase in saturation field with increasing pressure (Fig. 3.4b).

The dependence of intralayer magnetic exchange on bond geometry is more complex, as the intralayer exchange interactions in CrSBr involve a competition between FM superexchange interactions and weaker AFM direct exchange interactions. With increasing pressure, the magnitude of direct exchange should increase for J_1, J_2 and J_3, as all Cr–Cr distances ($d_{\mathrm{Cr-Cr}}$) shrink. These changes should be most pronounced for J_1 and J_2, which have experimentally determined $d_{\mathrm{Cr-Cr}}$ of ~3.51 and ~3.59 Å, respectively, whereas $d_{\mathrm{Cr-Cr}}$ for J_3 is much larger (~4.76 Å). The decreasing $d_{\mathrm{Cr-Cr}}$ increases the overlap of 3d orbitals between Cr atoms, resulting in the enhancement of the antiferromagnetic couplings in the direct exchange. As a result, the overall ferromagnetic couplings for J_1 and J_2 are weakened. The behavior of J_3 under pressure can be explained by the predicted structural changes, according to the Goodenough–Kanamori–Anderson rules.[74–76] An increase in the Cr–S1–Cr bond (θ_3) towards 180° should increase the contribution of antiferromagnetic exchange pathways, which weakens the overall ferromagnetic coupling. Because $d_{\mathrm{Cr-Cr}}$ remains well outside the range of Cr–Cr bonding for all pressures studied here, we would expect the direct exchange interactions to remain small relative to superexchange interactions, which agrees with our experimental and computational data where the net intralayer coupling remains FM.

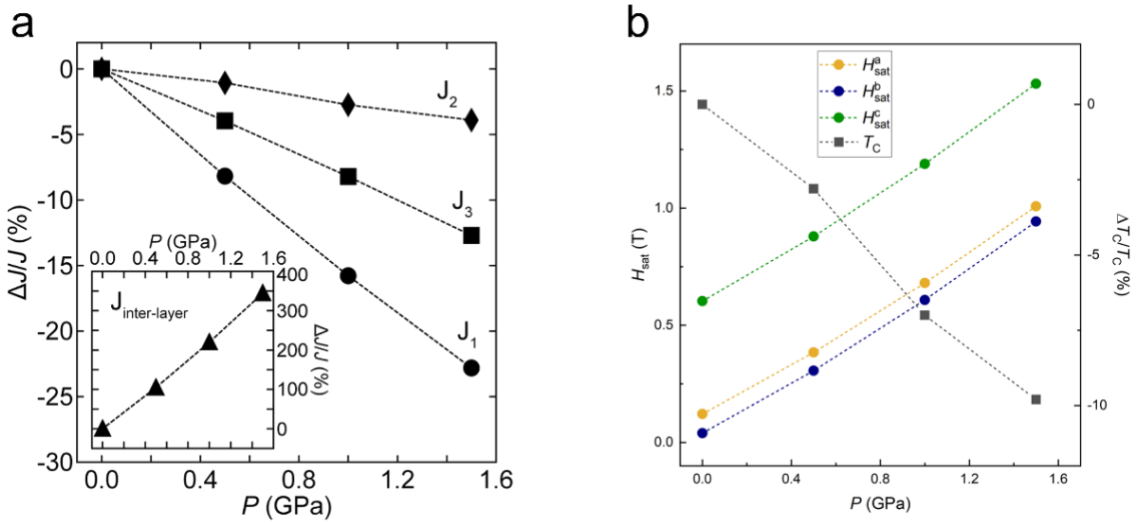

Figure 3.4 Pressure dependent magnetic couplings, saturation fields and magnetic ordering temperature. (a) Calculated percentage change in intralayer magnetic couplings versus P. Inset: calculated percentage change in J_{inter} versus P. (b) Calculated H_{sat} (left axis, orange, purple, and green dots) and T_C (right axis, black dots) versus P.

3.3 Summary

In summary, we find uniaxial strain and hydrostatic pressure as effective tuning knobs to control the magnetic properties of layered magnets. With uniaxial strain applied along the intermediate axis, an AFM to FM transition is obtained with a critical strain of ~0.5% along the intermediate axis. Under hydrostatic pressure, the ordering temperature is reduced due to the suppression of intralayer FM interactions resulting from the compression of the lattice, while saturation fields along the three crystal axes increase due to an increase in interlayer magnetic exchange energy.

3.4 Technical Details

The lattice structure of CrSBr was relaxed with the same method employed in Chapter 2. The calculated interlayer distance for bulk CrSBr is 8.011 Å. The applied uniaxial strain was calculated in percentile relative to the equilibrium structure. For each strain, the energy differences between the interlayer AFM and FM phases were calculated within the local spin density approximation (LSDA). We note that the calculated value of critical strain can be affected by factors such as the choice of pseudopotential used in the calculations. We find that an on-site Hubbard U correction is not needed to reproduce the correct magnetic ground-state properties of bulk CrSBr.

For each hydrostatic pressure applied, the intra- and interlayer Heisenberg magnetic exchange couplings J were calculated in 3×3×1 and 3×3×2 supercells respectively, by a four-state mapping method[73] within LSDA. The Curie temperature was calculated using metropolis Monte Carlo methods implemented in the VAMPIRE package.[78] The critical exponent was determined by fitting the temperature dependent normalized magnetization $m(T)$ to the Curie-Bloch equation in the classical limit $m(T) = \left(1 - \frac{T}{T_C}\right)^{\beta}$. The saturation fields along different axes were extracted based on the Heisenberg model $H = H_0 + H_{\text{inter}} - g\mu_B \sum_i h \cdot \mathbf{S}_i$, where $H_{\text{inter}} = \sum_{i\in t, j\in b} J_{\text{inter}} \mathbf{S}_i \cdot \mathbf{S}_j$. Here t and b denote the top and bottom layers in a unit cell, h represents the external magnetic field. The ground state energy differences between the FM and AFM states under different hydrostatic pressure were calculated with spin-orbit coupling taken into account within LSDA, based on the structures revealed by PBE-D2.

Chapter 4

Engineering Magnetic Phases of Layered Antiferromagnets by Interfacial Charge Transfer

Compared with magnetic phase transition controlled by structural engineering, such as applying strain, pressure, and shifting stacking orders, interfacial charge transfer offers an easier and more universal control knob that can enable robust switching of the interlayer magnetism in 2D magnets. In this chapter, we propose a new strategy to control the interlayer magnetic interactions by engineering the band alignment and charge transfer at the interfaces between vdW magnets and other vdW materials. We select bilayer CrSBr/monolayer graphene (biCrSBr/G) heterostructure as a novel platform to demonstrate the controllable interlayer magnetism in CrSBr.

4.1 Interfacial Charge Transfer in CrSBr/Graphene Heterostructure

To calculate the biCrSBr/G heterostructure from first principle, we employ a 5×1 supercell of CrSBr bilayer and an 8×2 supercell of graphene monolayer, resulting in nearly commensurate top and bottom layers. In this supercell, the *a* and *b* axes of CrSBr are aligned along the armchair and zigzag directions of graphene, respectively (Fig. 4.1a).

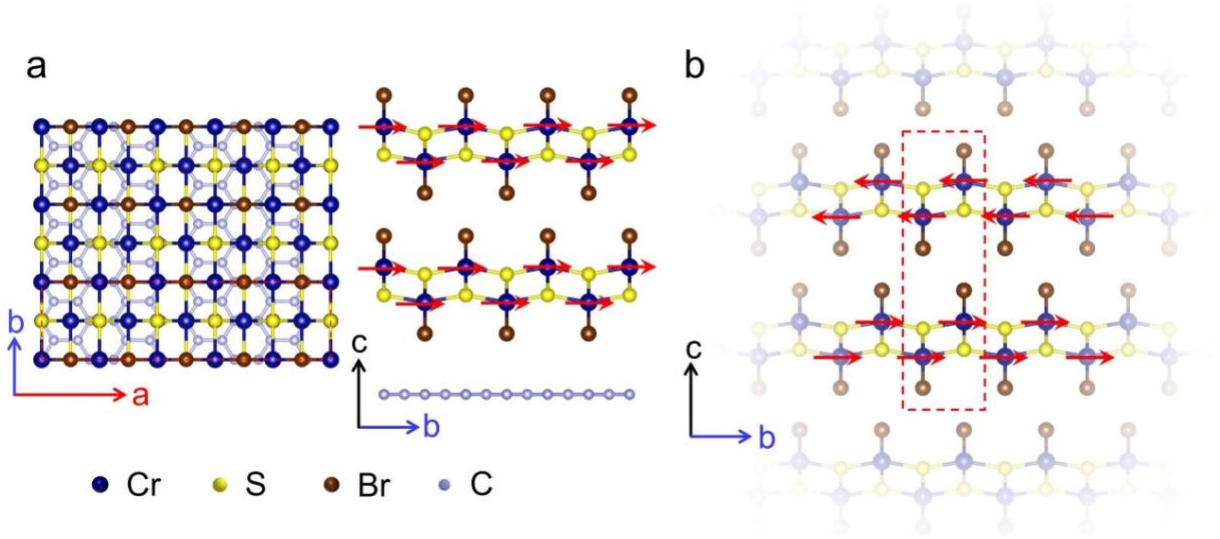

Figure 4.1 Schematic of crystal and magnetic structures for bilayer CrSBr/monolayer graphene heterostructure. (a) Crystal structure for the biCrSBr/G heterostructure in a supercell. CrSBr bilayer is stacked directly on graphene monolayer with the *a* and *b* axes of CrSBr aligned along the armchair and zigzag directions of graphene, respectively. The strain on graphene is <5%. Top and side views are shown on the left and right, respectively. (b) Side-view crystal and magnetic structures for CrSBr, a typical A-type layered van der Waals magnet. The system is ferromagnetic within each layer, and antiferromagnetically coupled between neighboring layers. The unit cell is marked by red dashed rectangular.

In contrast to its AFM ground state in the freestanding CrSBr bilayer, the calculated ground state of CrSBr bilayer in the biCrSBr/G heterostructure becomes FM (Fig. 4.1a). The calculated energy difference between the FM and AFM states $\Delta E = E_{\mathrm{FM}} - E_{\mathrm{AFM}}$ changes from 0.12 meV in the freestanding bilayer to -0.07 meV per unit cell ($Cr_4S_4Br_4$) upon stacking. We note that the calculated $\Delta E = 0.12$ meV for the freestanding bilayer is in good agreement with the experimental measurement of the critical field of 0.134 T along the easy axis *b*, which suggests $\Delta E =$

0.09 meV.[1] We further investigate the electronic properties of the heterostructure. The reciprocal space geometry of monolayer graphene, bilayer CrSBr and the biCrSBr/G heterostructure is shown in Fig. 4.2a. The corners (labeled K_G) in the hexagonal Brillouin zone (BZ) of graphene unit cells are folded onto the Γ–Y path in the rectangular BZ of the biCrSBr/G heterostructure, marked by K in the shaded rectangular of Fig. 4.2a. The band structures of the FM biCrSBr/G heterostructure for majority and minority spins are plotted along a BZ *k*-path (Γ–X–S–Y–Γ) in Fig. 4.2b and 4.2c, respectively, colored by a layer localization function defined as $\eta_n(\mathbf{k}) = \frac{\sum_{i\in \mathrm{Cr}}|\langle\psi_i|\phi_n(\mathbf{k})\rangle|^2 - \sum_{i\in \mathrm{G}}|\langle\psi_i|\phi_n(\mathbf{k})\rangle|^2}{\sum_{i\in \mathrm{Cr}}|\langle\psi_i|\phi_n(\mathbf{k})\rangle|^2 + \sum_{i\in \mathrm{G}}|\langle\psi_i|\phi_n(\mathbf{k})\rangle|^2}$, where n is band index and $\mathbf{k}$ is wavevector in reciprocal space. $\phi_n(\mathbf{k})$ and ψ_i denote the electron wave function and active atomic orbital i in the top CrSBr bilayer (Cr) or the bottom graphene monolayer (G). Therefore, $\eta_n(\mathbf{k}) = 1$ represents the wave function completely localized in the top CrSBr bilayer while $\eta_n(\mathbf{k}) = -1$ represents the wave function completely localized in the bottom graphene monolayer, marked by red and blue, respectively. The calculated band alignment between CrSBr bilayer and graphene monolayer shows that the Dirac point of graphene is higher than the conduction band minimum (CBM) of CrSBr bilayer by ~0.5 eV. This suggests significant interfacial charge transfer between CrSBr bilayer and graphene monolayer, and the electron density transferred from graphene monolayer to CrSBr bilayer is estimated to be ~$2.1 \times 10^{13}/\mathrm{cm}^2$ from Luttinger's theorem.[79,80]

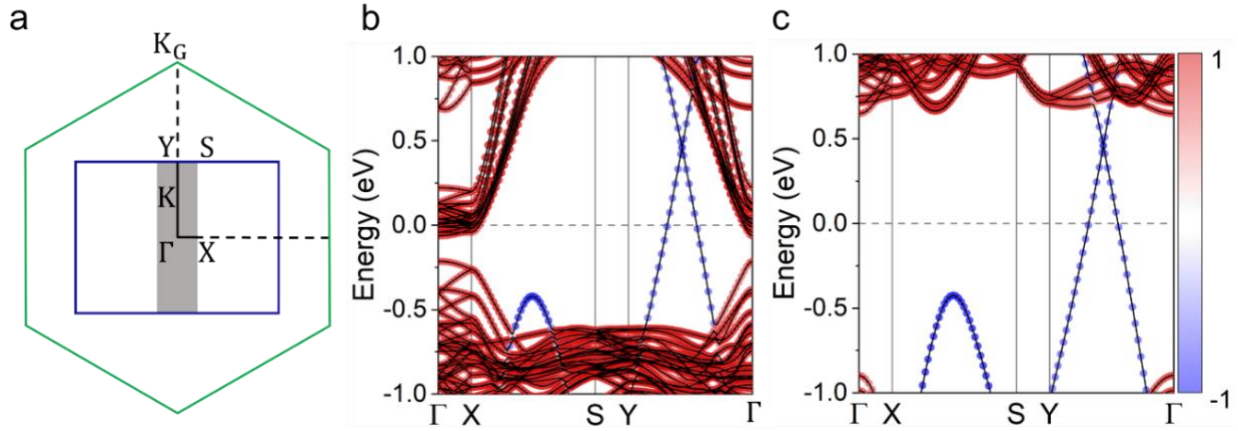

Figure 4.2 Calculated Kohn-Sham band structures of the FM biCrSBr/G heterostructure. (a) Schematic of the Brillouin zone (BZ) of graphene (green hexagonal), CrSBr (blue rectangular), and the biCrSBr/G supercell (grey shaded rectangular). The Dirac point (K_G) in the hexagonal BZ of graphene unit cell is folded onto Γ-Y path in the rectangular BZ of the biCrSBr/G heterostructure (marked by K). (b, c) Calculated Kohn-Sham band structures of the ferromagnetic biCrSBr/G heterostructure for (b) majority and (c) minority spins, respectively. The band wavefunction projection in CrSBr and graphene layers is marked by red and blue, respectively (see exact definition in main text). The Fermi level is shown by grey dashed lines. The charge transfer between the CrSBr/graphene interface is $\sim 2.1 \times 10^{13}/\mathrm{cm}^2$ from calculations.

To investigate the origin of the magnetic phase transition upon stacking, and whether the transition arises from the interfacial charge transfer, we calculate the carrier doping dependent ΔE between the collinear FM and AFM states for CrSBr bilayers without graphene. Fig. 4.3 shows that ΔE decreases almost linearly with increasing carrier density for both electron and hole, in the small carrier density regime ($< 3 \times 10^{12}/\mathrm{cm}^2$). This behavior suggests that both electron and hole doping favor the collinear FM phase over the AFM phase, and the doping leads to an AFM to FM magnetic phase transition. In CrSBr bilayers, the critical carrier density at phase transition for hole

doping ($0.8 \times 10^{12}/\mathrm{cm}^2$) is much smaller than that for electron doping ($2.4 \times 10^{12}/\mathrm{cm}^2$). Nonetheless, in the biCrSBr/G heterostructure, the electron carrier density in the CrSBr bilayer due to interfacial charge transfer (~$2.1 \times 10^{13}/\mathrm{cm}^2$) is an order of magnitude larger than the critical density. We therefore attribute the ferromagnetism in the biCrSBr/G heterostructure to the interfacial charge transfer, thanks to the band alignment between the two materials.

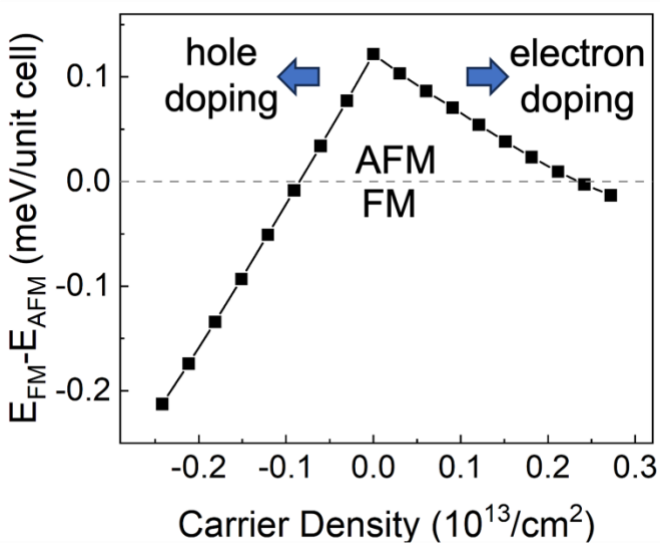

Figure 4.3 Calculated doping dependent magnetic ground state of bulk CrSBr. Magnetic ground state is defined by the energy difference between collinear FM and AFM bilayer CrSBr ($\Delta E = E_{\mathrm{FM}} - E_{\mathrm{AFM}}$). Positive (negative) carrier density refers to doped electron (hole) carrier density. Lines are guide to the eye. The AFM to FM magnetic phase transition occurs for both electron and hole doping.

To further exploit and control the magnetic phase transitions from interfacial charge transfer, we use open-shell molecules (e.g., NO_2) as admolecules to introduce charge carriers. For DFT calculations, a 3×3 supercell of the CrSBr bilayer is employed and Fig. 4.4 shows the entire structure. We find an FM magnetic ground state of the CrSBr bilayer with NO_2 adsorption at a

density of 1.1×10^{-10} mol/cm^2. This provides another route to achieve reversible magnetic phase transition in 2D magnets by molecular adsorption, as the initial undoped state can be recovered by annealing.[81]

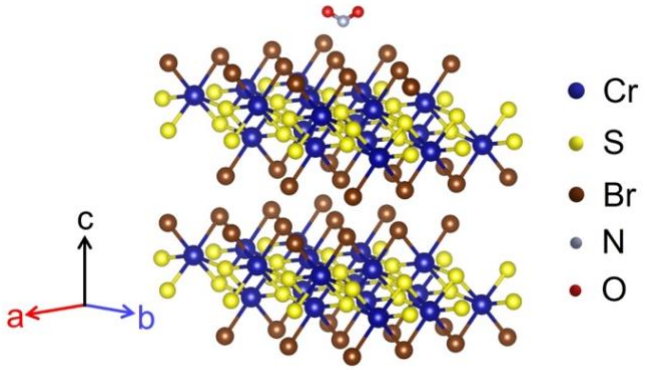

Figure 4.4 Crystal structure for NO_2 adsorbed on bilayer CrSBr. A 3×3 supercell of the CrSBr bilayer is adopted and the concentration of NO_2 is set to 1.1×10^{-10} mol/cm^2.

4.2 Carrier Doping Induced Ferromagnetism in Layered A-Type Magnets

To unveil the physical mechanism and general design strategy of magnetic phase transitions enabled by charge transfer, we construct an effective model consisting of ferromagnetic layers being electronically coupled, to describe layered A-type magnetic semiconductors including $MnBi_2Te_4$, CrX3, CrSBr, and $CrPS_4$.[38,58,62,82–84] The key to carrier doping induced ferromagnetism lies in the interlayer electronic coupling, i.e., electron (hole) hopping across the vdW interfaces. In this model, we include the frontier conduction bands (i.e., $|c_1(\mathbf{k})\rangle$ and $|c_2(\mathbf{k})\rangle$) or valance bands (i.e., $|v_1(\mathbf{k})\rangle$ and $|v_2(\mathbf{k})\rangle$) in the two adjacent layers as the basis (layer 1 and layer 2 in Fig. 4.5a). $E = E_c(\mathbf{k})$ or $E_v(\mathbf{k})$ is the eigenenergy of the corresponding frontier conduction or valence bands in each monolayer, respectively. $t = t_c(\mathbf{k})$ or $t_v(\mathbf{k})$ denotes the $\mathbf{k}$ dependent interlayer hopping between the degenerate conduction or valence bands, respectively. Considering the interlayer

wavefunction hybridization between these originally degenerate frontier bands, the Hamiltonian reads

$$H(\mathbf{k}) = \begin{pmatrix} E(\mathbf{k}) & t(\mathbf{k}) \\ t(\mathbf{k}) & E(\mathbf{k}) \end{pmatrix} \tag{4.1}$$

By solving the Hamiltonian in Eq. (4.1), bonding and anti-bonding states can be obtained as $E_{\pm}(\mathbf{k}) = E(\mathbf{k}) \pm t(\mathbf{k})$ (Fig. 4.5a). Therefore, with interlayer hybridization, $|c_1(\mathbf{k})\rangle$ and $|c_2(\mathbf{k})\rangle$ form bonding and anti-bonding orbitals with energy difference $2|t_c(\mathbf{k})|$, while $|v_1(\mathbf{k})\rangle$ and $|v_2(\mathbf{k})\rangle$ form bonding and anti-bonding orbitals with energy difference $2|t_v(\mathbf{k})|$.

The charge transfer process in the biCrSBr/G heterostructure can be treated equivalently as introducing carriers into a layered magnetic semiconductor. In the context of dilute doping, the energy difference between the FM and AFM phases changes by $-|(t_{\mathrm{FM}} - t_{\mathrm{AFM}})n|$, where hopping is evaluated at $\mathbf{k} = 0$. Here, n represents the number of charge carriers introduced to the system, and is measured by carrier density (cm^{-2}) for 2D materials in Fig. 4.3. Furthermore, we argue that $t_{\mathrm{AFM}} \sim 0$, as the interlayer hybridization between degenerate states in adjacent layers is suppressed by the interlayer AFM order (schematically illustrated in Fig. 4.5b). This suppression happens when spin-orbit coupling is weak, and the spinor of frontier band wavefunction is layer-polarized to the magnetization direction. As a result,

$$\Delta E(n) = \Delta E(n = 0) - |t_{\mathrm{FM}} n| \tag{4.2}$$

Here, $t_{\mathrm{FM}} = t_c(\mathbf{k} = 0)$ and $t_v(\mathbf{k} = 0)$ for electron and hole doping an FM bilayer, respectively. This effective model correctly reproduces the linear dependence of ΔE with carrier density from DFT calculations (Fig. 4.3). The slight decrease in the absolute value of the slope observed with increasing carrier density possibly results from the change of the interlayer hopping with $\mathbf{k}$. ΔE can be affected by additional factors, such as the interlayer electric polarization, which have not been included in the present model. Nonetheless, the FM state remains more stable than the AFM

state at the high doping level of biCrSBr/G. We note that the super-super-exchange interaction J that dictates $\Delta E(n = 0)$ is assumed to remain unchanged by doping, which applies to the dilute doping limit as we will show the next.

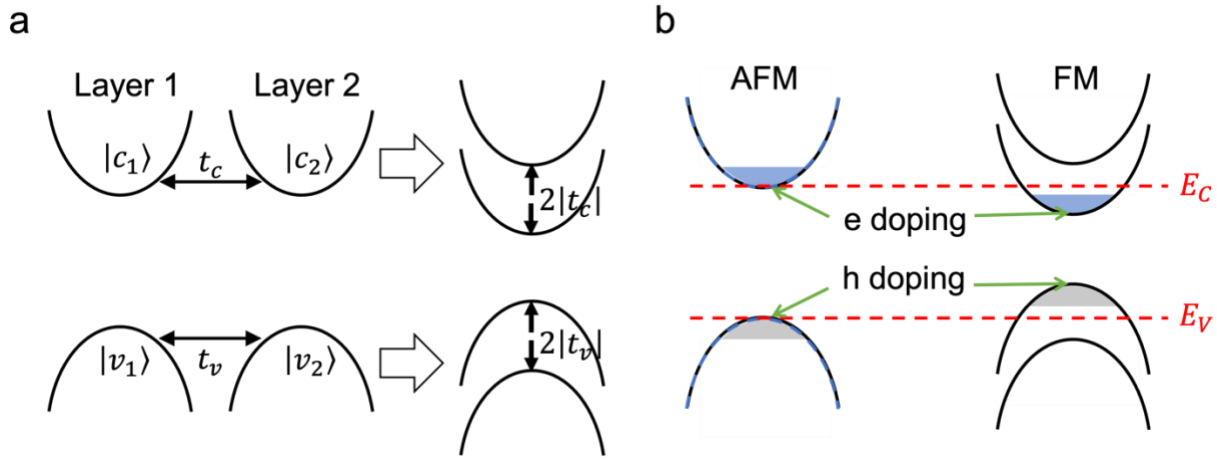

Figure 4.5 Schematic illustrations of the effective model for doping induced ferromagnetism in layered A-type magnets. (a) Schematic illustration of interlayer coupling in layered van der Waals magnets. Two neighboring layers are labeled by layer 1 and layer 2, with states $|c_1\rangle$, $|v_1\rangle$ and $|c_2\rangle$, $|v_2\rangle$ schematically shown by parabolic bands. t_c and t_v denote the interlayer hopping between degenerate conduction bands and valence bands, respectively. With interlayer hybridization, $|c_1\rangle$ and $|c_2\rangle$ form bonding and anti-bonding orbitals with energy difference $2|t_c|$, while $|v_1\rangle$ and $|v_2\rangle$ form bonding and anti-bonding orbitals with energy difference $2|t_v|$. (b) Schematic diagrams of electron (blue shaded area) and hole (grey shaded area) doping to AFM and FM layers. The red dashed lines represent the CBM and VBM (marked by E_C and E_V) in single layer, respectively.

Based on the model we have developed for doping induced magnetic phase transition in 2D layered magnets, the interlayer hopping at the FM state can be extracted from Fig. 4.3. By analyzing the slopes of ΔE vs. carrier density curves, we obtain: $t_{\mathrm{FM}}^{c} = 31$ meV and $t_{\mathrm{FM}}^{v} = 84$ meV in

accordance with Eq. (4.2) for bilayer CrSBr unit cell ($Cr_4S_4Br_4$). We further validate our effective model by comparing its parameters to the hopping obtained from DFT bands. Fig. 4.6 displays the calculated Kohn-Sham band structures for AFM and FM CrSBr bilayers with electron (hole) doping density of $0.6 \times 10^{12}/\mathrm{cm}^2$. For AFM CrSBr bilayers, the conduction and valence bands are doubly degenerate in spins, suggesting minimal interlayer hopping. For FM CrSBr bilayers, sizable band splitting is obtained at CBM and VBM. Therefore, the hopping term t_c corresponds to half of the band splitting between the second and first conduction bands (CB2 and CB1), while t_v is instead between the first and second valence bands (VB1 and VB2) at the zone center in the dilute doping limit, e.g., $t^c_{\mathrm{AFM}} = t^v_{\mathrm{AFM}} = 0$, and $t^c_{\mathrm{FM}} = 31\ \mathrm{meV}$, $t^v_{\mathrm{FM}} = 76\ \mathrm{meV}$, which agree reasonably well with those obtained based on the effective model. This agreement indicates that the model correctly describes the microscopic mechanism of magnetic phase transition and validates the assumption that the change of interlayer super-super exchange between localized Cr moments can be considered negligible with doping.

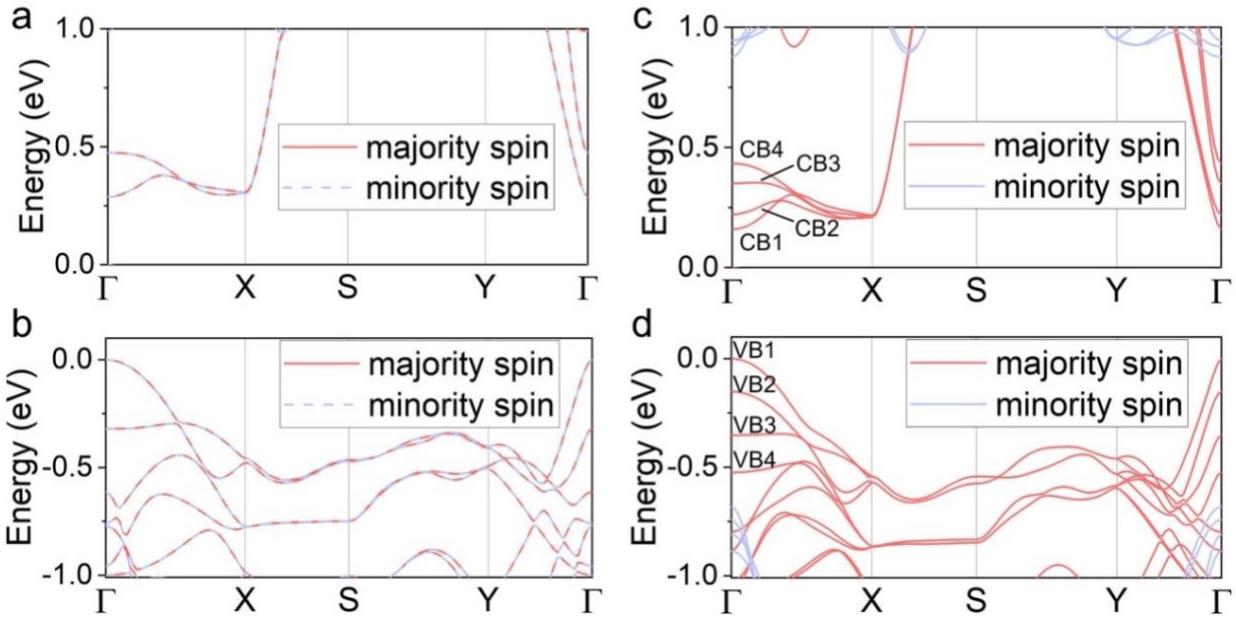

Figure 4.6 Calculated Kohn-Sham band structures with carrier doping. (a) AFM CrSBr bilayers with 0.6×10^{12} cm^{-2} electron doping, (b) AFM CrSBr bilayers with 0.6×10^{12} cm^{-2} hole doping, (c) FM CrSBr bilayers with 0.6×10^{12} cm^{-2} electron doping, d) FM CrSBr bilayers with 0.6×10^{12} cm^{-2} hole doping. Red and blue lines represent bands for majority and minority spins, respectively.

We further compare band structures with and without carrier doping, and confirm that the interlayer hopping for both AFM and FM CrSBr bilayers remain almost unchanged at DFT level with small amount of carrier doping. The strategy and model developed here can serve as a general approach for carrier induced tunable interlayer magnetic order beyond the biCrSBr/G heterostructure.

4.3 Spin Canting Transition with Carrier Doping in Layered A-Type Magnets

In anisotropic magnets, AFM to FM phase transitions (with magnetic field, strain, etc.) can happen with antiparallel magnetic moments continuously aligned to parallel, or suddenly flipped to parallel. To investigate which process occurs with carrier doping, we explicitly include interlayer exchange interactions and intralayer magnetic anisotropy in total energy. Without loss of generality, we take tri-axial anisotropy into account. The easy axis is set along *b*, following CrSBr. The carrier density dependent total energy per $Cr_2S_2Br_2$ is given by

$$E(n) = J\mathbf{S}_1 \cdot \mathbf{S}_2 + \sum_{i=1,2} A_a(S_i \cdot \hat{a})^2 - A_b\left(S_i \cdot \hat{b}\right)^2 + A_c(S_i \cdot \hat{c})^2 - |tn| \qquad (4.3)$$

Here, the first term refers to the interlayer magnetic exchange coupling, and $J > 0$ favors interlayer AFM states. $\mathbf{S}_1$ and $\mathbf{S}_2$ denote the spins of neighboring layers. The orientations of $\mathbf{S}_1$ and $\mathbf{S}_2$ are denoted by their tilt angles θ_1 and θ_2 with respect to the *b*-axis, and azimuthal angles ϕ_1 and ϕ_2 with respect to the *c*-axis, respectively. The second term describes the anisotropy energies, where $\hat{b}$, $\hat{a}$ and $\hat{c}$ are the easy, intermediate, and hard axes, respectively. For convenience, we set $A_a = 0$ and $A_{b,c} > 0$. The third term is from interlayer hopping of doped electrons (holes) as we discussed previously. The hopping integral $t = t_{\mathrm{FM}} \cos(\alpha/2)$, where $\alpha(\theta_1, \theta_2, \phi_1, \phi_2)$ is the angle between $\mathbf{S}_1$ and $\mathbf{S}_2$. The cosine form in t comes from the inner product of spinor wavefunctions across the vdW interface.[85,86]

We discover that the carrier induced AFM-to-FM phase transition is always a spin canting process. This can be understood at the small canting angle limit of Eq. (4.3), in which the energy gain from last term is $\sim\delta\alpha$, whereas the energy penalty from other terms is $\sim(\delta\alpha)^2$. To determine the exact spin configuration and magnetic ground state energy, we minimize E at each n by taking the partial derivative of Eq. (4.3),

$$\frac{\partial E}{\partial \theta_1} = \frac{\partial E}{\partial \theta_2} = \frac{\partial E}{\partial \phi_1} = \frac{\partial E}{\partial \phi_2} = 0 \tag{4.4}$$

For bilayer CrSBr, we use $J = 0.013$ meV, $A_b = 0.014$ meV, $A_c = 0.038$ meV obtained from DFT calculations, which are consistent with those fitted from experiments.[87] $t_{\mathrm{FM},c} = 31$ meV and $t_{\mathrm{FM},v} = 84$ meV are extracted from DFT results in accordance with Eq. (4.2) as shown above. The dependence of ground-state energy on carrier density is plotted in Fig. 4.7a, and the energies of easy-axis collinear AFM and FM states are also calculated for comparison. With increasing carrier density, the ground-state energy varies smoothly until a sudden change of slope at a critical carrier density n_c, which is given by $t_{\mathrm{FM}} n_c = 4S^2\sqrt{J + A_b}\left(\sqrt{J + A_b} - \sqrt{A_b}\right)$. Therefore, we obtain $n_c^e \sim 2.6 \times 10^{12}/\mathrm{cm}^2$ and $n_c^h \sim 1.0 \times 10^{12}/\mathrm{cm}^2$ for transitioning into FM in the cases of electron and hole doping, respectively. To understand the structures of $\mathbf{S}_1$ and $\mathbf{S}_2$ during this process, we plot $\alpha(n)$ in Fig. 4.7b. With increasing carrier density, the originally antiparallel $\mathbf{S}_1$ and $\mathbf{S}_2$ gradually tilt away from the easy axis (*b*-axis) in the *ab*-plane until $n = n_c$. In the canting process, $\mathbf{S}_1$ and $\mathbf{S}_2$ become noncolinear but remain symmetric to the intermediate axis (*a*-axis). At $n = n_c$, the system suddenly transits to the FM state with $\mathbf{S}_1$ and $\mathbf{S}_2$ aligned along the easy axis. For bilayer CrSBr, the critical transition happens at $\alpha_c \sim 147°$.

To validate the carrier doping induced spin canting transition process in bilayer CrSBr obtained by our model with tri-axial anisotropy, we perform DFT calculations with spin-orbit coupling included for different doping levels ($n < n_c$) in the CrSBr bilayer. Fig. 4.7c illustrates the energy variations with respect to α. For each doping level, $\mathbf{S}_1$ and $\mathbf{S}_2$ are noncolinear but remain symmetric to the intermediate axis *a*. At finite doping, the energy of the system will initially decrease and then increase with increasing α. With increasing carrier density, α of the ground state decreases, indicating that $\mathbf{S}_1$ and $\mathbf{S}_2$ tilt away from the easy axis *b* for the ground state. Comparing

Fig.4.7b and c, we can conclude that the critical angles from DFT calculations agrees reasonably well with the results from our model.

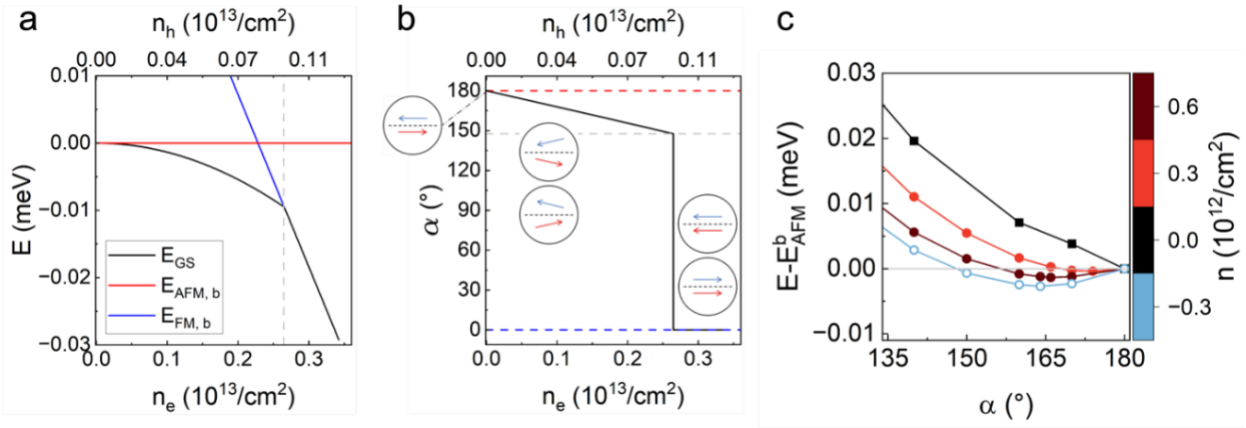

Figure 4.7 Carrier doping induced magnetic phase transition with noncollinear spins. (a) Carrier density (n_e and n_h for electron and hole, respectively) dependent ground state energy E_{GS} (black solid line) for bilayer CrSBr. The energy of AFM ($E_{\mathrm{AFM},\,b}$) and FM ($E_{\mathrm{FM},\,b}$) states with spins collinear to the easy axis are plotted in red and blue solid lines for reference, with $E_{\mathrm{AFM},\,b}$ set to 0. The critical doping density is represented by grey dashed line. (b) Carrier density dependent canting angle between spins of neighboring layers for bilayer CrSBr. The corresponding spin configurations are shown schematically by insets. The critical angle is shown by grey dashed line. (c) The dependence of energy on the angle α between constraint spins of neighboring layers at different doping levels for bilayer CrSBr from DFT calculations with spin-orbit coupling. Crimson, red, black, and blue colors denote doping levels of 0.6×10^{12} cm^{-2} electron doping, 0.3×10^{12} cm^{-2} electron doping, without doping and 0.3×10^{12} cm^{-2} hole doping, respectively. $\mathbf{S}_1$ and $\mathbf{S}_2$ are noncolinear but remain symmetric to the intermediate axis a.

We expand the discussion to generic A-type 2D magnets with different hard axis anisotropy and interlayer hopping, in which the range of canting angles can be significantly different. In

accordance with Eq. (4.3), the canting angle is controlled by two independent and unitless parameters, $t_{\mathrm{FM}}n/JS^2$ and A_b/J. Here we firstly focus on systems with A_b and J comparable in magnitude. Our results in Fig. 4.8a show that, within the $A_b > J$ regime, for systems with weak anisotropy and strong interlayer coupling, spins of neighboring layers can develop very large canting angle. Fig. 4.8b illustrates the role of magnetic anisotropy on the critical angle and critical carrier density. For systems with large anisotropy ($A_b \gg J$), the magnetic phase transition will approach a spin-flip transition at $t_{\mathrm{FM}}n_c \sim 2JS^2$. Next, we consider the more complicated case where the anisotropy is relatively weak, i.e., $A_b \ll J$. Surprisingly, an intermediate state emerges between the *a*-axis symmetric canting process and the FM state along the *b*-axis, as depicted in Fig. 4.8c. With increasing carrier density, the originally antiparallel $\mathbf{S}_1$ and $\mathbf{S}_2$ gradually tilt away from the easy axis *b* in the *ab*-plane until $n = n_{c1}$, remaining symmetric to the intermediate axis *a*, and then suddenly transit to the intermediate state with $\mathbf{S}_1$ and $\mathbf{S}_2$ symmetric to the *b*-axis. In the intermediate state, the spins will tilt to the easy axis *b* and finally experience a sudden transit to the FM state with spins aligned along the easy axis at $n = n_{c2}$. The critical carrier density n_{c1} and n_{c2} are given by $t_{\mathrm{FM}}n_{c1} = 2S^2\sqrt{2(J + A_b)(J - A_b)}$ and $t_{\mathrm{FM}}n_{c2} = 4S^2(J - A_b)$, respectively.

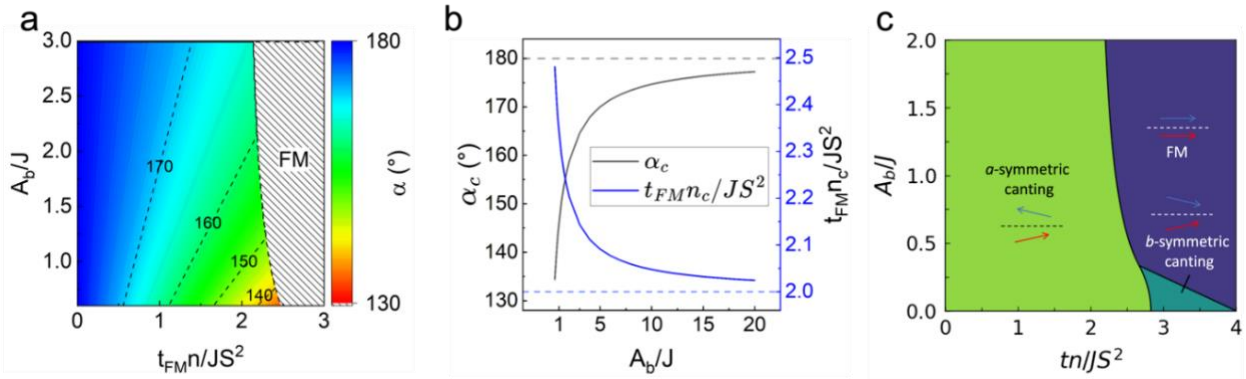

Figure 4.8 Hopping and magnetic anisotropy controlled magnetic ground state phase diagram. (a) Doping and anisotropy dependent canting angle between spins of neighboring layers in hard-axis A-type 2D magnets. $t_{\mathrm{FM}}n/JS^2$ and A_b/J reflect the effects of doping and anisotropy, respectively. (b) Anisotropy dependent critical angle (left) and critical carrier density (right). (c) Full magnetic ground state phase diagram determined by doping and magnetic anisotropy with small anisotropy included. For each phase, the corresponding spin configuration of neighboring layers is shown schematically by inset.

4.4 Conclusions

In summary, we have proposed heterostructures consisting of vdW magnets and nonmagnetic layered materials for controlling interlayer magnetism in 2D magnets and demonstrated that carrier doping gives dominant contributions to the tunability of interlayer magnetism in heterostructures with proper band alignment through first-principles calculations. This holds true for not only type-III heterojunctions with the magnetic layers, but also metals of which the Fermi level is higher than the CBM or lower than the VBM of the magnetic layers. We have built an effective model to elaborate the interlayer hopping difference between the interlayer AFM and FM states as the underlying physical mechanism for the AFM to FM magnetic phase transition observed with both electron and hole doping. By including magnetic anisotropy in our model, we have found that the

doping induced AFM to FM transition is a spin canting process with critical carrier density. Besides interfacial charge transfer in heterostructures, electrostatic doping can be achieved through molecular adsorption or gating, making it an accessible and effective method to control interlayer magnetism in experiments. Our findings not only provide a general framework for understanding charge transfer induced magnetic phase transition in vdW magnets, but also offer a versatile approach to modulating magnetism in 2D magnets *via* interfacial charge transfer, which paves the way for realizing spintronics at the atomically thin level.

4.5 Computational Methods

The lattice structure of CrSBr was relaxed with the same method employed in Chapter 2. The lattice constant *a* was relaxed to 2.457 Å in monolayer graphene. The biCrSBr/G heterostructure was constructed with a 5×1 CrSBr supercell stacked on top of an 8×2 graphene supercell, where the *a* and *b* axes of CrSBr bilayer are aligned along the armchair and zigzag directions of graphene monolayer, respectively. The graphene monolayer experiences tensile strain of ~3% along the armchair direction, and compressive strain of ~4% along the zigzag direction. We note that the strain is introduced to ensure a commensurate structure in supercell calculations, and graphene can hardly sustain compressive strain without buckling.[88] However, as the AFM to FM phase transition results from charge transfer, the phase transition should remain robust for arbitrary stacking geometry between bilayer CrSBr and graphene. The vdW spatial gap between bottom CrSBr layer (from bottom Br atoms) and graphene monolayer is 3.380 Å. A vacuum region of 15 Å was added in the out-of-plane direction to avoid interaction between periodic images. An 8×30×1 *k*-grid was used for Brillouin zone sampling in the biCrSBr/G heterostructure. A dipole correction was applied in all the calculations for biCrSBr/G heterostructures.[89] The band structures and the ground state

energies for each carrier density with electron (hole) doping were calculated within LSDA. The carrier density was tuned by changing the total number of electrons in the unit cell, with a compensating jellium background of opposite charge. A 120×90×1 *k*-grid was used for Brillouin zone sampling to converge the magnetic moment at the dilute doping (in a bilayer unit cell without graphene). For magnetic anisotropy, spin-orbit coupling was included at the fully-relativistic level. A Gaussian smearing of 1 meV was adopted for electron occupation.

Chapter 5

Ultrafast Optical Control of Excitonic Structures in Low-Dimensional Materials

Advances in optics have often stemmed from the discovery and optimization of novel materials with tailored optical properties. A recent frontier in this field is coherent preparation, which facilitates remarkable changes in the optical properties of materials. Within the realm of quantum optics and photonics, electromagnetically induced transparency (EIT) emerges as an important phenomenon and has garnered extensive attention due to its capacity for coherent manipulation of material optical properties.[90,91] EIT refers to the cancellation of the linear response at resonance by destructive interference in a laser-dressed medium. At its core, EIT often involves three-level quantum systems, arranged in either a lambda, ladder or V configuration. Typically, the excitonic structure of such a system includes two bare states (the ground state $|g\rangle$ and an excited state $|e_1\rangle$) coupled by a metastable state $|e_2\rangle$, as depicted schematically in Fig. 5.1b for the "ladder" configuration. In this chapter, our focus is on the application of electromagnetic fields within the optical frequency range, resonant with the transitions in a three-level system with the ladder configuration. For consistency, states are labeled so that the $|g\rangle \leftrightarrow |e_2\rangle$ transition is always dipole-forbidden. When illuminated by two laser beams, the states $|g\rangle$ and $|e_1\rangle$ are coupled by the probe beam, while the states $|e_1\rangle$ and $|e_2\rangle$ are coupled by the coupling beam, where $|e_1\rangle$ is assumed to be the only decaying state and thus the only way to absorption. Because the coupling field is significantly more intense than the probe field, the probability amplitudes for the direct ($|g\rangle$-$|e_1\rangle$) and indirect ($|g\rangle$-$|e_1\rangle$-$|e_2\rangle$-$|e_1\rangle$ or its higher order variants) absorption pathways are of equal

magnitude but opposite sign, when the two laser beams resonant with the transitions.[92] Subsequently, this gives rise to a transparency resonance which is sensitive to the properties of the transitions. As EIT is closely related to other nonlinear optical effects and extremely sensitive to external perturbations, it emerges as a potent tool for applications ranging from optical switching to light propagation controlling and quantum information processing.

5.1 Formalism of EIT in a Three-Level System

We now turn to a detailed examination of the structure for the laser-dressed eigenstates within a ladder-type three-level system, as illustrated in Fig. 5.1b. The most extensively studied example of such a system is the so-called Rydberg atom (shown in Fig. 5.1c, with experimental setup schematically shown in Fig. 5.1a), which displays rich many-body behavior due to their enhanced dipole-dipole interactions.[93,94] In Rydberg atoms, the three levels are composed of the ground state, an excited state and highly excited Rydberg states (named in analogy to the hydrogenic Rydberg series of energy levels). Besides Rydberg atoms, we identify atomically thin layers of van der Waals materials as promising candidates for implementing three-level systems, attributable to the strong light-matter interactions arising from their reduced dimensionality.[95] In addition, we propose a novel three-level system in a vdW layered material, consisting of the ground state and two closely spaced excited states where one is optically bright and the other remains dark (Fig. 5.1d), which can be found in CrSBr layers.

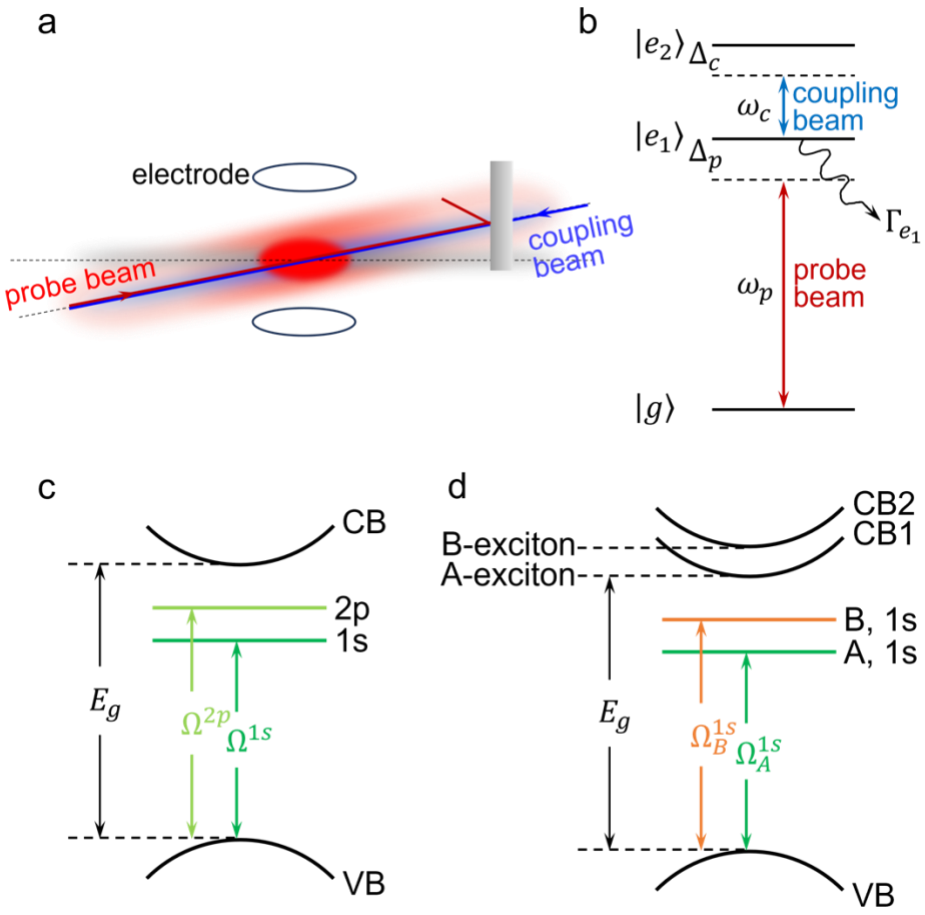

Figure 5.1 Examples for ladder-type three-level systems. (a) A schematic of the experimental setup. (b) Schematic of a typical ladder three-level system with states represented by $|g\rangle$, $|e_1\rangle$ and $|e_2\rangle$. $|g\rangle$ and $|e_1\rangle$ are coupled by a probe beam of frequency ω_p, while $|e_1\rangle$ and $|e_2\rangle$ are coupled by a coupling beam of frequency ω_c. Δ_p and Δ_c denote the probe and coupling beam detunings from atomic resonances, respectively. Γ_{ik} denote the radiative decay rates from state $|i\rangle$ to state $|k\rangle$. (c) Energy level diagram of the ladder system with Rydberg excitons. A pair of valence band and conduction band with bandgap E_g hosting Rydberg excitons are schematically represented by parabolic bands. The three levels consist of the ground state, exciton 1s and 2p states. (d) Energy level diagram of the ladder system with two excitons (labeled A and B) originating from different

band pairs (VB-CB1 and VB-CB2). The three levels are composed of the ground state, A exciton 1*s* state and B exciton 1*s* state.

Within the dipole approximation, the atom-laser interaction, given by $H_{\text{int}} = -\boldsymbol{\mu} \cdot \boldsymbol{E}$, is often expressed in terms of the Rabi frequency $\Omega = \boldsymbol{\mu} \cdot \boldsymbol{E}_0$, where $\boldsymbol{E}_0$ is the amplitude of the electromagnetic field $\boldsymbol{E}$, and $\boldsymbol{\mu}$ is the transition dipole moment. Therefore, the Hamiltonian of such a three-level system interacting with a coupling beam with real Rabi frequency Ω_c and a probe beam with Rabi frequency Ω_p under the rotating-wave approximation in Schrödinger picture leads to (in atomic units $\hbar = m = e = 1$)

$$H_{\text{int}} = -\frac{1}{2}\begin{pmatrix} 0 & \Omega_p & 0 \\ \Omega_p & -2\Delta_p & \Omega_c \\ 0 & \Omega_c & -2(\Delta_p + \Delta_c) \end{pmatrix} \tag{5.1}$$

where ω_g is set to 0. $\Delta_p = \omega_{e_1} - \omega_p$ and $\Delta_c = \omega_{e_2} - \omega_c$ denote the detunings of the probe and coupling beams from atomic resonances, respectively. The dynamics of laser-driven systems are governed by the master equation for the density matrix ρ

$$\dot{\rho} = -i[H_{\text{int}}, \rho] + \mathcal{L}(\rho) \tag{5.2}$$

where the Lindblad operator $\mathcal{L}$ accounts for the decay and dephasing processes of the excited states given by e.g.,

$$\mathcal{L}_{e_1 g}(\rho) = -\frac{\Gamma_{e_1 g}}{2}\left(\sigma_{e_1 g}\sigma_{g e_1}\rho - \sigma_{g e_1}\rho\sigma_{e_1 g} + \text{h. c.}\right) \tag{5.3}$$

where $\Gamma_{e_1 g}$ represents the spontaneous decay rate of state $|e_1\rangle$. Evaluating the master equation at steady state ($\dot{\rho} = 0$) with a weak probe field ($\Omega_p \ll \Omega_c$, $\rho_{gg} \sim 1$), we obtain the expressions for the off-diagonal density-matrix elements $\rho_{jk=g,e_1,e_2}$ and hence the linear susceptibility $\chi^{(1)}$ as following

$$\rho_{e_1 g} \approx \frac{i\Omega_p \gamma_{e_2 g}}{\gamma_{e_1 g}\gamma_{e_2 g} + \Omega_c^2}, \rho_{31} \approx \frac{-\Omega_p \Omega_c}{\gamma_{e_1 g}\gamma_{e_2 g} + \Omega_c^2}$$

$$\chi^{(1)} = \frac{4\pi N \left|\mu_{g e_1}\right|^2 \rho_{e_1 g}}{\Omega_p} \tag{5.4}$$

where N is the density of excitons. We define the rates $\gamma_{e_1 g} = \Gamma_{e_1 g} + 2i\Delta_p$ and $\gamma_{e_2 g} = \gamma' + 2i(\Delta_p + \Delta_c)$, with γ' corresponding to the dephasing rate of the Rydberg state. The linear susceptibility $\chi^{(1)}$ given in Eq. (5.4) encapsulates many key features of EIT, as its real and imaginary components describe the dispersion and absorption properties, respectively. To decide the change of absorption due to the appearance of dressed states, it is essential to get accurate estimations of the transition dipole moments for both intra- and inter-exciton transitions with excitonic effects considered. To this end, we establish a formalism capable of calculating the desired transition dipole moments at the GW-BSE level

$$\begin{aligned} \hat{\lambda} \cdot \langle S|\boldsymbol{\mu}|S'\rangle &= |q|\hat{\lambda} \cdot \langle S|-\boldsymbol{r_e} + \boldsymbol{r_h}|S'\rangle \\ &= \frac{|q|\hat{\lambda}}{i(\Omega_S - \Omega_{S'})}(-\langle S|\boldsymbol{v_e}|S'\rangle + \langle S|\boldsymbol{v_h}|S'\rangle) \end{aligned} \tag{5.5}$$

Here $\hat{\lambda}$ denotes the polarization vector of the beam and $\boldsymbol{v}$ is the velocity operator. The excitation energy (Ω_S) is the eigenvalue of an exciton eigenstate $|S\rangle$ from the BSE method. Applying the above formalism to real material systems, we demonstrate the control of excitonic structures using ultrafast optical technique and the realization of EIT in atomically thin layers through *ab initio* calculations at the GW-BSE level combined with parameters fitted from previous experiments.

5.2 Intra-exciton Transitions and EIT Simulations in Monolayer $MoSe_2$

Firstly, $MoSe_2$ is investigated as a prototypical two-dimensional material hosting Rydberg excitons for a possible ladder-type three-level system, where Rydberg excitons are formed due to the

significant enhancement of the Coulomb interactions in 2D. Previous research has reported Autler–Townes doublets observed in monolayer $MoSe_2$.[96] In this work, we utilize *ab initio* GW-BSE calculations (details in Methods) to capture the excitonic structure of monolayer $MoSe_2$. As shown in Fig. 5.2a, our calculations reveal a direct quasiparticle bandgap of ~2.28 eV at the *K* (*K′*) valley in monolayer $MoSe_2$, incorporating a strong self-energy correction of ~0.80 eV compared to the bandgap obtained at the DFT-LDA level. Solving the first-principles BSE, we find a series of strongly-bound exciton Rydberg states with excitation energies located below the quasiparticle bandgap, as illustrated in the exciton energy levels in Fig. 5.2b. Meanwhile, exciton wavefunctions for the first three exciton states (1*s*, $2p_+$, $2p_-$) are plotted in the first Brillouin zone (FBZ), which are centered around the *K* (*K′*) point. The exciton binding energy for the 1*s* exciton is calculated to be ~0.41 eV. These findings align well with those reported in previous studies.[97]

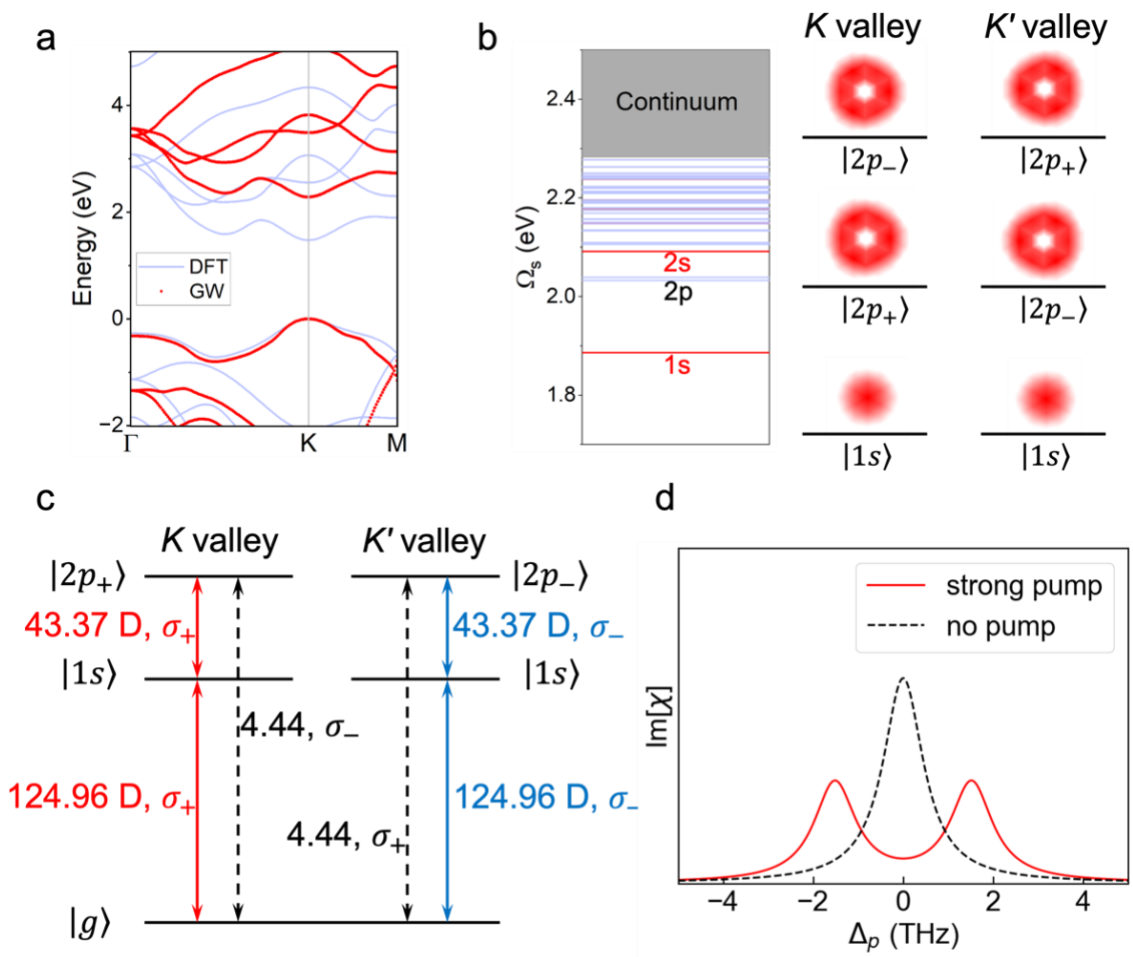

Figure 5.2 First-principles GW-BSE calculations and simulations for monolayer $MoSe_2$. (a) Kohn-Sham band structures from DFT-LDA method (blue solid lines) and quasiparticle band structures from the GW method (red dots) for monolayer $MoSe_2$. The quasiparticle bandgap is roughly 2.3 eV. (b) Exciton energy levels (left) and exciton envelope functions in *k*-space (right) for the lowest-energy transition Rydberg series calculated using GW-BSE method. Optically bright (dark) exciton states are colored by red (blue). Exciton envelope function amplitudes for exciton 1*s* state with $\Omega_S^{1s} = 1.886$ eV and two $2p$ states with $\Omega_S^{2p_\pm}\left(\Omega_S^{2p_\mp}\right) = 2.033$ eV and 2.039 eV are plotted centered around the *K* (*K′*) point in the FBZ. (c) Illustration of the selection rules for the three-level system in monolayer $MoSe_2$ consisting of Rydberg excitons in the *K* and *K′* valleys. The transition dipole moments for 1*s*, $2p_+$ ($2p_-$) and intra-exciton transition $1s \leftrightarrow 2p_+$ ($2p_-$) are labeled

for the K (K') valley. (d) simulated EIT absorption spectrum with strong coupling field ($\Omega_c = 1.52$ THz, red solid line) and without pump ($\Omega_c \sim 0$, black dashed line).

We further elucidate the exciton fine structure of monolayer $MoSe_2$ by highlighting the simplified exciton energy spectrum of the 1s and 2p exciton states in Fig. 5.2c. Notably, the 2p exciton states exhibit energy splitting with opposite ordering for the K and K' valleys due to the opposite chirality in each valley. We label the two 2p states as 2p_+ and 2p_-, where transition 1s↔2p_+ (2p_-) can be coherently driven by $\sigma_+(\sigma_-)$-polarized infrared radiation from the 1s state (σ_+ and σ_- denote left- and right-handed circular polarization, respectively). The energy splitting between the 2p_+ and 2p_- exciton states is ~6 meV in a single valley, with the sign reversed between K and K' valleys. Such valley-dependent exciton fine structure, which reflects important wavefunction properties derived from the Bloch band geometry, significantly influences intra-excitonic light-matter interactions. Utilizing the formalism developed at the GW-BSE level in Section 5.1, we have calculated the transition dipole moments for the 1s, 2p_+ (2p_-) and intra-exciton transition 1s↔2p_+ (2p_-) for the K (K') valley to be approximately 125.0, 4.4 and 43.4 Debye, respectively. Based on Eq. (5.4) and the transition dipole moments obtained from our formalism, we simulate the photoinduced changes in the 1s exciton absorption ($\chi^{(1)}$) of monolayer $MoSe_2$ for the K valley using σ_+ optical probe, where the 1s↔2p_+ intra-exciton transition is coherently driven by a σ_+-polarized coupling beam. Our simulations assume the driving photon energy closely matches the 1s↔2p_+ transition ($\Delta_c \sim 0$) and is strongly off-resonant from the interband transition. Parameters such as the local optical field strength E_0 (70 ± 10 kV cm^{-1}), decay rates γ_{1s} (4.8 meV) and γ_{2p_+}(4.5 meV) are adopted from parameters fitted from previous experimental results, reported by F. Wang *et al.* (2019).[96] Fig. 5.2d shows the simulated imaginary component of the scaled optical susceptibility, dependent on the

probe field detuning (Δ_p) without pump and with strong coupling field. A transparency "window" emerges at resonance in the simulated absorption spectrum, indicating the realization of EIT in monolayer $MoSe_2$.

5.3 Intra- and Inter-exciton Transitions in Layered CrSBr

Next, we shift our focus to CrSBr, a novel material system with two closely spaced excited states originating from different interband transitions. As a typical A-type magnetic semiconductor, the extensive tunability of the interlayer magnetic coupling makes CrSBr a fertile ground for exploring light-matter interactions and magneto-optical phenomena in the 2D limit. As illustrated in Fig 3.a, monolayer CrSBr displays highly anisotropic spin-polarized bands and semiconducting quasiparticle bandgap of ~1.81 eV from first-principles GW calculations. CBM and VBM appear at the Γ point and share the same spin orientation. The first two conduction bands, labeled CBM1 and CBM2, are nearly degenerate at the GW level. The transition from VBM to CBM1 is parity-allowed, whereas the transition to CBM2 is parity-forbidden.

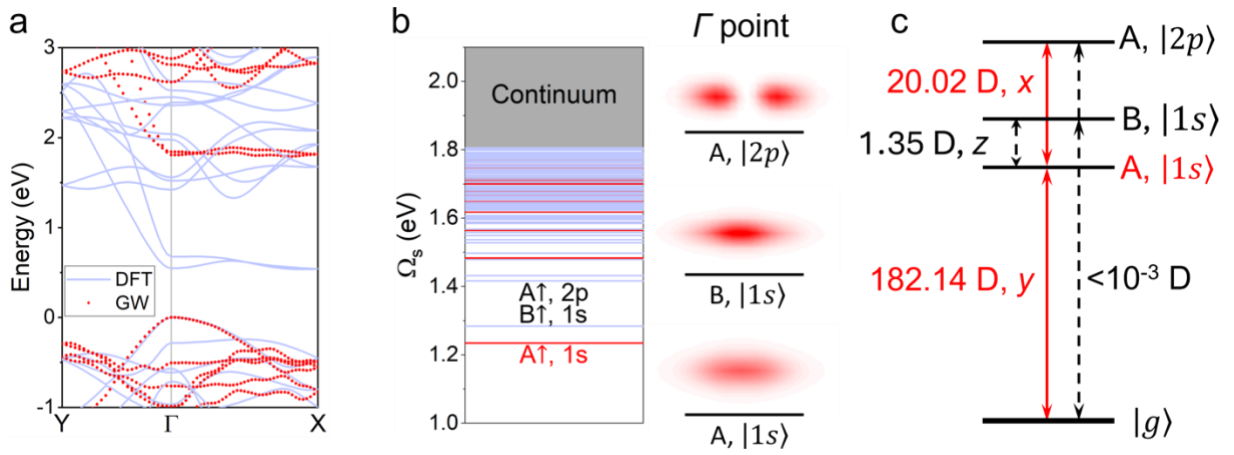

Figure 5.3 First-principles GW-BSE calculations and simulations for monolayer CrSBr. (a) Kohn-Sham band structures from DFT-PBE method (blue solid lines) and quasiparticle band structures from the GW method (red dots) for monolayer CrSBr. The quasiparticle bandgap is roughly 1.8 eV. The bands of majority spins are shown (those of minority spins have much larger gaps). (b) Exciton energy levels (left) and exciton envelope functions in *k*-space (right) obtained from GW-BSE calculation. Optically bright (dark) exciton states are colored by red (blue). Exciton envelope function amplitudes for A exciton 1s state with $\Omega_S^{1s} = 1.235$ eV, 2p state with $\Omega_S^{2p} = 1.416$ eV, and B exciton 1s state with $\Omega_S^{1s} = 1.284$ eV are plotted centered around the Γ point in the FBZ. (c) Illustration of the selection rules for the exciton states in monolayer CrSBr consisting of Rydberg excitons around the Γ point. The transition dipole moments for A 1s, A 2p, B 1s, intra- and inter-exciton transitions A 1s↔2p and A 1s↔B 1s are labeled. The transitions are linearly polarized.

We gain further insights into the exciton fine structure of monolayer CrSBr through GW-BSE calculations. Fig. 5.3b displays the exciton wavefunctions in the FBZ alongside the diagram of exciton energies. The two lowest-energy excitons, labeled A and B, have calculated exciton binding energies of approximately 0.61 and 0.52 eV for a free-standing monolayer, respectively.

Exciton A is associated with the interband transition VBM–CBM1, while exciton B is linked to the interband transition from VBM to the more dispersive CBM2 along the Γ–Y direction in *k*-space, resulting in a smaller exciton radius for B along k_y. The transition dipole moments for the A 1*s*, A 2*p*, B 1*s* states, intra- and inter-exciton transitions A 1*s*↔2*p* and A 1*s*↔B 1*s* have been derived using our formalism and are indicated in the simplified exciton energy spectrum in Fig. 5.3c. Only the A exciton 1*s* state and the intra-exciton transition 1*s*↔2*p* are dipole-allowed, with transition dipole moments of roughly 182.1 and 20.0 Debye, exhibiting linear polarization along the *y*- and *x*-axes, respectively. Similar to monolayer $MoSe_2$, the Rydberg series of A exciton in monolayer CrSBr offers a viable platform for realizing EIT in atomically thin layers. Moreover, the distinct band structure featuring VBM–CBM1–CBM2 with corresponding selection rules also identifies a potential candidate for a ladder-type three-level system in the CrSBr system and hence we turn to pristine bilayer CrSBr with the AFM ground state.

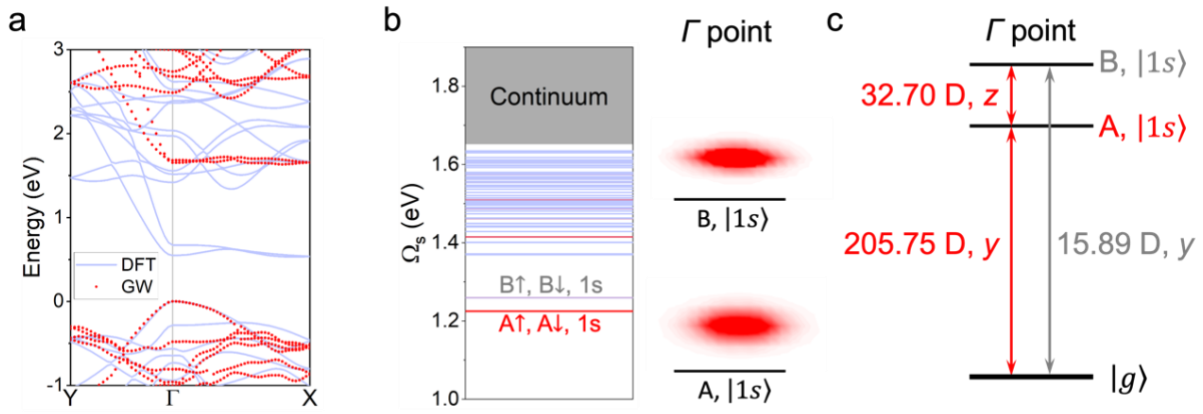

Figure 5.4 First-principles GW-BSE calculations and simulations for AFM bilayer CrSBr. (a) Kohn-Sham band structures from DFT-PBE (blue solid lines) and quasiparticle band structures from the GW method (red dots) for the AFM CrSBr bilayer. Bands are degenerate in spin with a quasiparticle bandgap of roughly 1.7 eV. (b) Exciton energy levels (left) and exciton envelope functions in *k*-space (right) obtained from *ab initio* GW-BSE calculation. Exciton envelope function amplitudes for A and B exciton 1*s* states with $\Omega_S^A = 1.225$ eV and $\Omega_S^B = 1.259$ eV, respectively, are plotted centered around the Γ point in the FBZ. (c) Illustration of the selection rules for the three-level system in bilayer CrSBr consisting of two (A and B) exciton series. The transition dipole moments for A 1*s*, B 1*s*, and inter-exciton transition A 1*s*↔B 1*s* are labeled. The transitions are linearly polarized.

As shown in Fig. 5.4a, the bands are degenerate in spin for the AFM bilayer. The GW-BSE calculations unveil the nature of the optical transitions, as depicted in Fig. 5.4b. The dominant optical transitions arise from the two-fold degenerate lowest-energy excitons in the CrSBr bilayers, with the calculated exciton binding energies of ~0.46 eV for a free-standing AFM bilayer. In this AFM bilayer configuration, the lowest-energy bright excitons correspond to the A exciton in the monolayer case with twofold degeneracy (splitting <0.5 meV), as the two layers are virtually

decoupled due to the AFM ordering. Similarly, the second lowest-energy dark excitons are also doubly degenerate, associated with the B exciton in the monolayer case. The transition dipole moments for the A 1*s*, B 1*s* states and A 1*s*↔B 1*s* transition are calculated using our formalism and highlighted in the simplified exciton energy spectrum in Fig. 5.4c. Notably, the transition A 1*s*↔B 1*s* is dipole-allowed, creating a ladder-type three-level system involving the ground state, A 1*s* and B 1*s* states. As a result, the dark (B) and bright (A) excitons can be coherently coupled by an optical field, leading to modifications in the absorption features as a function of frequency.

5.4 Conclusions

In summary, we have developed an effective approach to engineer excitonic structures and achieve EIT in 2D materials using ultrafast optical fields. Applying first-principles GW-BSE calculations and simulations to 2D materials including $MoSe_2$ and CrSBr, we have found the originally dark exciton can be coherently coupled to the optically bright exciton, resulting in an almost complete suppression of absorption at resonance controllable through the strength of the control field. We have established a comprehensive physical framework that underpins the formalism for simulating EIT at the GW-BSE level and demonstrated that the manipulation of medium transparency is feasible at the atomic scale. By leveraging the manipulation of quantum states and the precise dynamical control over light-matter interactions, EIT in 2D materials is predicted to be a powerful tool for advancing technologies in quantum sensing, computing and communication, underscoring the profound capabilities of quantum optical phenomena.

5.5 Computational Details

The mean-field starting point of the GW calculations were performed using DFT implemented in the QUANTUM ESPRESSO package,[8] with norm-conserving pseudopotentials employed.[67] The plane-wave kinetic energy cutoffs of the pseudopotentials are 80 Ry for $MoSe_2$ and 85 Ry for CrSBr. For structural relaxation, we employed the PBE-D2 functional.[68] The structures were fully relaxed until the force on each atom was <0.005 eV/Å. The lattice constant *a* was relaxed to 3.31 Å in monolayer $MoSe_2$. The lattice constants for CrSBr were calculated to be 3.51 and 4.71 Å along the *a* and *b* axes, respectively, and the interlayer distance (Cr-Cr) was calculated to be 8.09 Å in bilayer CrSBr.

The GW[15] calculations were carried out using the BerkeleyGW package[18] at the G_0W_0 level. A truncated Coulomb interaction was used along the out-of-plane direction to avoid interactions between the free-standing $MoSe_2$ (CrSBr) layer and its periodic images.[98] For $MoSe_2$, the wavefunctions and band structures were calculated within the LDA.[10,11] The size of the supercell in the out-of-plane direction was set to be 16 Å. The dielectric matrix was constructed with a total of 2,000 bands and a cutoff energy of 35 Ry for the screened exchange in the calculation of the electron self-energy. The dielectric matrix and the self-energy were calculated on a 6×6×1 *q*-grid with 10 subsampling points.[69] A static remainder approach was used in the self-energy calculation.[70] The exciton energy levels and wavefunctions were calculated using the GW-BSE method.[17] The exciton interaction kernel was calculated on a 72×72×1 *k*-grid onto a round patch of *k*-points centered at the *K* (*K′*) valley of radius 0.12 $Å^{-1}$, as the exciton wavefunctions are localized in the reciprocal space. For CrSBr, the wavefunctions and band structures were calculated within PBE. Spin-polarized calculations were adopted for CrSBr. The sizes of the supercell in the out-of-plane direction were set to be 16 and 28 Å for the monolayer and bilayer CrSBr, respectively.

The dielectric matrix was constructed with a cutoff energy of 35 Ry in the calculation of the electron self-energy. The dielectric matrix and the self-energy were calculated on an 8×6×1 q-grid. Ten subsampling points along the in-plane diagonal of the supercell were included in the calculation of the dielectric function. A static remainder approach was used, together with 1,700 bands in the bilayer calculation. The exciton energy levels and wavefunctions were calculated using the GW-BSE methods with the exciton interaction kernel calculated on a 32×24×1 k-grid in bilayer.

Bibliography

1. Wilson, N. P. *et al.* Interlayer electronic coupling on demand in a 2D magnetic semiconductor. *Nat. Mater.* **20**, 1657–1662 (2021).

2. Cenker, J. *et al.* Reversible strain-induced magnetic phase transition in a van der Waals magnet. *Nat. Nanotechnol.* **17**, 256–261 (2022).

3. Telford, E. J. *et al.* Designing Magnetic Properties in CrSBr through Hydrostatic Pressure and Ligand Substitution. *Adv. Phys. Res.* **2**, 2300036 (2023).

4. Xie, K., Zhang, X.-W., Xiao, D. & Cao, T. Engineering Magnetic Phases of Layered Antiferromagnets by Interfacial Charge Transfer. *ACS Nano* **17**, 22684–22690 (2023).

5. Hohenberg, P. & Kohn, W. Inhomogeneous Electron Gas. *Phys. Rev.* **136**, B864–B871 (1964).

6. Kohn, W. & Sham, L. J. Self-Consistent Equations Including Exchange and Correlation Effects. *Phys. Rev.* **140**, A1133–A1138 (1965).

7. Kresse, G. & Furthmüller, J. Efficient iterative schemes for ab initio total-energy calculations using a plane-wave basis set. *Phys. Rev. B* **54**, 11169–11186 (1996).

8. Giannozzi, P. *et al.* QUANTUM ESPRESSO: a modular and open-source software project for quantum simulations of materials. *J. Phys. Condens. Matter* **21**, 395502 (2009).

9. Born, M. & Oppenheimer, R. Zur Quantentheorie der Molekeln. *Ann. Phys.* **389**, 457–484 (1927).

10. Ceperley, D. M. & Alder, B. J. Ground State of the Electron Gas by a Stochastic Method. *Phys. Rev. Lett.* **45**, 566–569 (1980).

11. Perdew, J. P. & Zunger, A. Self-interaction correction to density-functional approximations for many-electron systems. *Phys. Rev. B* **23**, 5048–5079 (1981).

12. Perdew, J. P. & Wang, Y. Accurate and simple analytic representation of the electron-gas correlation energy. *Phys. Rev. B* **45**, 13244–13249 (1992).

13. Perdew, J. P., Burke, K. & Ernzerhof, M. Generalized Gradient Approximation Made Simple. *Phys. Rev. Lett.* **77**, 3865–3868 (1996).

14. Hedin, L. New Method for Calculating the One-Particle Green's Function with Application to the Electron-Gas Problem. *Phys. Rev.* **139**, A796–A823 (1965).

15. Hybertsen, M. S. & Louie, S. G. Electron correlation in semiconductors and insulators: Band gaps and quasiparticle energies. *Phys. Rev. B* **34**, 5390–5413 (1986).

16. Strinati, G. Application of the Green's functions method to the study of the optical properties of semiconductors. *Riv. Nuovo Cimento 1978-1999* **11**, 1–86 (1988).

17. Rohlfing, M. & Louie, S. G. Electron-hole excitations and optical spectra from first principles. *Phys. Rev. B* **62**, 4927–4944 (2000).

18. Deslippe, J. *et al.* BerkeleyGW: A massively parallel computer package for the calculation of the quasiparticle and optical properties of materials and nanostructures. *Comput. Phys. Commun.* **183**, 1269–1289 (2012).

19. Gonze, X. *et al.* ABINIT: First-principles approach to material and nanosystem properties. *Comput. Phys. Commun.* **180**, 2582–2615 (2009).

20. Marini, A., Hogan, C., Grüning, M. & Varsano, D. yambo: An ab initio tool for excited state calculations. *Comput. Phys. Commun.* **180**, 1392–1403 (2009).

21. Pines, D. & Bohm, D. A Collective Description of Electron Interactions: II. Collective vs Individual Particle Aspects of the Interactions. *Phys. Rev.* **85**, 338–353 (1952).

22. Bohm, D. & Pines, D. A Collective Description of Electron Interactions: III. Coulomb Interactions in a Degenerate Electron Gas. *Phys. Rev.* **92**, 609–625 (1953).

23. Ehrenreich, H. & Cohen, M. H. Self-Consistent Field Approach to the Many-Electron Problem. *Phys. Rev.* **115**, 786–790 (1959).

24. Albrecht, S., Reining, L., Del Sole, R. & Onida, G. Ab Initio Calculation of Excitonic Effects in the Optical Spectra of Semiconductors. *Phys. Rev. Lett.* **80**, 4510–4513 (1998).

25. Rohlfing, M. & Louie, S. G. Electron-Hole Excitations in Semiconductors and Insulators. *Phys. Rev. Lett.* **81**, 2312–2315 (1998).

26. Onida, G., Reining, L. & Rubio, A. Electronic excitations: density-functional versus many-body Green's-function approaches. *Rev. Mod. Phys.* **74**, 601–659 (2002).

27. Bistritzer, R. & MacDonald, A. H. Moiré bands in twisted double-layer graphene. *Proc. Natl. Acad. Sci.* **108**, 12233–12237 (2011).

28. Cao, Y. *et al.* Unconventional superconductivity in magic-angle graphene superlattices. *Nature* **556**, 43–50 (2018).

29. Cao, Y. *et al.* Correlated insulator behaviour at half-filling in magic-angle graphene superlattices. *Nature* **556**, 80–84 (2018).

30. Wilson, N. P., Yao, W., Shan, J. & Xu, X. Excitons and emergent quantum phenomena in stacked 2D semiconductors. *Nature* **599**, 383–392 (2021).

31. Mak, K. F. & Shan, J. Semiconductor moiré materials. *Nat. Nanotechnol.* **17**, 686–695 (2022).

32. Huang, B. *et al.* Layer-dependent ferromagnetism in a van der Waals crystal down to the monolayer limit. *Nature* **546**, 270–273 (2017).

33. Gong, C. *et al.* Discovery of intrinsic ferromagnetism in two-dimensional van der Waals crystals. *Nature* **546**, 265–269 (2017).

34. Gibertini, M., Koperski, M., Morpurgo, A. F. & Novoselov, K. S. Magnetic 2D materials and heterostructures. *Nat. Nanotechnol.* **14**, 408–419 (2019).

35. Sivadas, N., Okamoto, S., Xu, X., Fennie, Craig. J. & Xiao, D. Stacking-Dependent Magnetism in Bilayer CrI_3. *Nano Lett.* **18**, 7658–7664 (2018).

36. Huang, B. *et al.* Electrical control of 2D magnetism in bilayer CrI_3. *Nat. Nanotechnol.* **13**, 544–548 (2018).

37. Li, S. *et al.* Magnetic-Field-Induced Quantum Phase Transitions in a van der Waals Magnet. *Phys. Rev. X* **10**, 011075 (2020).

38. Peng, Y. *et al.* Magnetic Structure and Metamagnetic Transitions in the van der Waals Antiferromagnet $CrPS_4$. *Adv. Mater.* **32**, 2001200 (2020).

39. Klein, J. *et al.* The Bulk van der Waals Layered Magnet CrSBr is a Quasi-1D Material. *ACS Nano* **17**, 5316–5328 (2023).

40. Jiang, S., Li, L., Wang, Z., Mak, K. F. & Shan, J. Controlling magnetism in 2D CrI_3 by electrostatic doping. *Nat. Nanotechnol.* **13**, 549–553 (2018).

41. Song, T. *et al.* Switching 2D magnetic states via pressure tuning of layer stacking. *Nat. Mater.* **18**, 1298–1302 (2019).

42. Chen, W. *et al.* Direct observation of van der Waals stacking–dependent interlayer magnetism. *Science* **366**, 983–987 (2019).

43. Hejazi, K., Luo, Z.-X. & Balents, L. Noncollinear phases in moiré magnets. *Proc. Natl. Acad. Sci.* **117**, 10721–10726 (2020).

44. Wang, C., Gao, Y., Lv, H., Xu, X. & Xiao, D. Stacking Domain Wall Magnons in Twisted van der Waals Magnets. *Phys. Rev. Lett.* **125**, 247201 (2020).

45. Xu, Y. *et al.* Coexisting ferromagnetic–antiferromagnetic state in twisted bilayer CrI_3. *Nat. Nanotechnol.* **17**, 143–147 (2022).

46. Ramasubramaniam, A. Large excitonic effects in monolayers of molybdenum and tungsten dichalcogenides. *Phys. Rev. B* **86**, 115409 (2012).

47. Komsa, H.-P. & Krasheninnikov, A. V. Effects of confinement and environment on the electronic structure and exciton binding energy of MoS_2 from first principles. *Phys. Rev. B* **86**, 241201 (2012).

48. Qiu, D. Y., da Jornada, F. H. & Louie, S. G. Optical Spectrum of MoS_2: Many-Body Effects and Diversity of Exciton States. *Phys. Rev. Lett.* **111**, 216805 (2013).

49. Liu, Y. *et al.* Van der Waals heterostructures and devices. *Nat. Rev. Mater.* **1**, 1–17 (2016).

50. Burch, K. S., Mandrus, D. & Park, J.-G. Magnetism in two-dimensional van der Waals materials. *Nature* **563**, 47–52 (2018).

51. Zhang, Y. *et al.* Direct observation of a widely tunable bandgap in bilayer graphene. *Nature* **459**, 820–823 (2009).

52. Li, G. *et al.* Observation of Van Hove singularities in twisted graphene layers. *Nat. Phys.* **6**, 109–113 (2010).

53. Jiang, T. *et al.* Valley and band structure engineering of folded MoS_2 bilayers. *Nat. Nanotechnol.* **9**, 825–829 (2014).

54. Liu, K. *et al.* Evolution of interlayer coupling in twisted molybdenum disulfide bilayers. *Nat. Commun.* **5**, 4966 (2014).

55. Ju, L. *et al.* Tunable excitons in bilayer graphene. *Science* **358**, 907–910 (2017).

56. van der Zande, A. M. *et al.* Tailoring the Electronic Structure in Bilayer Molybdenum Disulfide via Interlayer Twist. *Nano Lett.* **14**, 3869–3875 (2014).

57. Telford, E. J. *et al.* Layered Antiferromagnetism Induces Large Negative Magnetoresistance in the van der Waals Semiconductor CrSBr. *Adv. Mater.* **32**, 2003240 (2020).

58. Lee, K. *et al.* Magnetic Order and Symmetry in the 2D Semiconductor CrSBr. *Nano Lett.* **21**, 3511–3517 (2021).

59. Jiang, Z., Wang, P., Xing, J., Jiang, X. & Zhao, J. Screening and Design of Novel 2D Ferromagnetic Materials with High Curie Temperature above Room Temperature. *ACS Appl. Mater. Interfaces* **10**, 39032–39039 (2018).

60. Guo, Y., Zhang, Y., Yuan, S., Wang, B. & Wang, J. Chromium sulfide halide monolayers: intrinsic ferromagnetic semiconductors with large spin polarization and high carrier mobility. *Nanoscale* **10**, 18036–18042 (2018).

61. Wang, H., Qi, J. & Qian, X. Electrically tunable high Curie temperature two-dimensional ferromagnetism in van der Waals layered crystals. *Appl. Phys. Lett.* **117**, 083102 (2020).

62. McGuire, M. A., Dixit, H., Cooper, V. R. & Sales, B. C. Coupling of Crystal Structure and Magnetism in the Layered, Ferromagnetic Insulator CrI_3. *Chem. Mater.* **27**, 612–620 (2015).

63. McGuire, M. A. Crystal and Magnetic Structures in Layered, Transition Metal Dihalides and Trihalides. *Crystals* **7**, 121 (2017).

64. Wang, C. *et al.* A family of high-temperature ferromagnetic monolayers with locked spin-dichroism-mobility anisotropy: MnNX and CrCX (X = Cl, Br, I; C = S, Se, Te). *Sci. Bull.* **64**, 293–300 (2019).

65. Wu, M., Li, Z., Cao, T. & Louie, S. G. Physical origin of giant excitonic and magneto-optical responses in two-dimensional ferromagnetic insulators. *Nat. Commun.* **10**, 2371 (2019).

66. Li, L. *et al.* Black phosphorus field-effect transistors. *Nat. Nanotechnol.* **9**, 372–377 (2014).

67. Hamann, D. R. Optimized norm-conserving Vanderbilt pseudopotentials. *Phys. Rev. B* **88**, 085117 (2013).

68. Grimme, S. Semiempirical GGA-type Density Functional Constructed with a Long-Range Dispersion Correction. *J. Comput. Chem.* **27**, 1787–1799 (2006).

69. da Jornada, F. H., Qiu, D. Y. & Louie, S. G. Nonuniform sampling schemes of the Brillouin zone for many-electron perturbation-theory calculations in reduced dimensionality. *Phys. Rev. B* **95**, 035109 (2017).

70. Deslippe, J., Samsonidze, G., Jain, M., Cohen, M. L. & Louie, S. G. Coulomb-hole summations and energies for GW calculations with limited number of empty orbitals: A modified static remainder approach. *Phys. Rev. B* **87**, 165124 (2013).

71. Mak, K. F., Shan, J. & Ralph, D. C. Probing and controlling magnetic states in 2D layered magnetic materials. *Nat. Rev. Phys.* **1**, 646–661 (2019).

72. Li, T. *et al.* Pressure-controlled interlayer magnetism in atomically thin CrI_3. *Nat. Mater.* **18**, 1303–1308 (2019).

73. Xiang, H., Lee, C., Koo, H.-J., Gong, X. & Whangbo, M.-H. Magnetic properties and energy-mapping analysis. *Dalton Trans.* **42**, 823–853 (2012).

74. Goodenough, J. B. Theory of the Role of Covalence in the Perovskite-Type Manganites [La, M(II)]MnO3. *Phys. Rev.* **100**, 564–573 (1955).

75. Goodenough, J. B. An interpretation of the magnetic properties of the perovskite-type mixed crystals $La_{1-x}Sr_xCoO_{3-\lambda}$. *J. Phys. Chem. Solids* **6**, 287–297 (1958).

76. Kanamori, J. Superexchange interaction and symmetry properties of electron orbitals. *J. Phys. Chem. Solids* **10**, 87–98 (1959).

77. Scheie, A. *et al.* Spin Waves and Magnetic Exchange Hamiltonian in CrSBr. *Adv. Sci.* **9**, 2202467 (2022).

78. Evans, R. F. L. *et al.* Atomistic spin model simulations of magnetic nanomaterials. *J. Phys. Condens. Matter* **26**, 103202 (2014).

79. Luttinger, J. M. Fermi Surface and Some Simple Equilibrium Properties of a System of Interacting Fermions. *Phys. Rev.* **119**, 1153–1163 (1960).

80. Luttinger, J. M. & Ward, J. C. Ground-State Energy of a Many-Fermion System. II. *Phys. Rev.* **118**, 1417–1427 (1960).

81. Schedin, F. *et al.* Detection of individual gas molecules adsorbed on graphene. *Nat. Mater.* **6**, 652–655 (2007).

82. Gong, Y. *et al.* Experimental Realization of an Intrinsic Magnetic Topological Insulator*. *Chin. Phys. Lett.* **36**, 076801 (2019).

83. Li, J. *et al.* Intrinsic magnetic topological insulators in van der Waals layered $MnBi_2Te_4$-family materials. *Sci. Adv.* **5**, eaaw5685 (2019).

84. Cai, X. *et al.* Atomically Thin $CrCl_3$: An In-Plane Layered Antiferromagnetic Insulator. *Nano Lett.* **19**, 3993–3998 (2019).

85. Anderson, P. W. & Hasegawa, H. Considerations on Double Exchange. *Phys. Rev.* **100**, 675–681 (1955).

86. de Gennes, P.-G. Effects of Double Exchange in Magnetic Crystals. *Phys. Rev.* **118**, 141–154 (1960).

87. Diederich, G. M. *et al.* Tunable interaction between excitons and hybridized magnons in a layered semiconductor. *Nat. Nanotechnol.* **18**, 23–28 (2023).

88. Zhang, Y. & Liu, F. Maximum asymmetry in strain induced mechanical instability of graphene: Compression versus tension. *Appl. Phys. Lett.* **99**, 241908 (2011).

89. Bengtsson, L. Dipole correction for surface supercell calculations. *Phys. Rev. B* **59**, 12301–12304 (1999).

90. Harris, S. E., Field, J. E. & Imamoğlu, A. Nonlinear optical processes using electromagnetically induced transparency. *Phys. Rev. Lett.* **64**, 1107–1110 (1990).

91. Boller, K.-J., Imamoğlu, A. & Harris, S. E. Observation of electromagnetically induced transparency. *Phys. Rev. Lett.* **66**, 2593–2596 (1991).

92. Fleischhauer, M., Imamoglu, A. & Marangos, J. P. Electromagnetically induced transparency: Optics in coherent media. *Rev. Mod. Phys.* **77**, 633–673 (2005).

93. Friedler, I., Petrosyan, D., Fleischhauer, M. & Kurizki, G. Long-range interactions and entanglement of slow single-photon pulses. *Phys. Rev. A* **72**, 043803 (2005).

94. Mohapatra, A. K., Jackson, T. R. & Adams, C. S. Coherent Optical Detection of Highly Excited Rydberg States Using Electromagnetically Induced Transparency. *Phys. Rev. Lett.* **98**, 113003 (2007).

95. Chernikov, A. *et al.* Exciton Binding Energy and Nonhydrogenic Rydberg Series in Monolayer WS_2. *Phys. Rev. Lett.* **113**, 076802 (2014).

96. Yong, C.-K. *et al.* Valley-dependent exciton fine structure and Autler–Townes doublets from Berry phases in monolayer $MoSe_2$. *Nat. Mater.* **18**, 1065–1070 (2019).

97. Zhang, C. *et al.* Probing Critical Point Energies of Transition Metal Dichalcogenides: Surprising Indirect Gap of Single Layer WSe_2. *Nano Lett.* **15**, 6494–6500 (2015).

98. Ismail-Beigi, S. Truncation of periodic image interactions for confined systems. *Phys. Rev. B* **73**, 233103 (2006).